



An entropy-variables-based formulation of residual distribution schemes for non-equilibrium flows



Jesús Garicano-Mena ^{a,b,*}, Andrea Lani ^b, Gérard Degrez ^{b,c}

^a E.T.S. Ingeniería Aeronáutica y del Espacio, Universidad Politécnica de Madrid Plaza del Cardenal Cisneros, 3, Madrid, 28040, Spain

^b von Karman Institute for Fluid Dynamics, Waterloose Steenweg, 72, Sint-Genesius-Rode, 1640, Belgium

^c Service Aéro-Thermo-Mécanique, Université Libre de Bruxelles, Avenue F.D. Roosevelt, 50, Bruxelles, 1050, Belgium

ARTICLE INFO

Article history:

Received 27 July 2017

Received in revised form 8 February 2018

Accepted 10 February 2018

Available online 15 February 2018

Keywords:

Computational fluid dynamics

Residual distribution schemes

Hypersonic flow

Entropy variables

Thermo-chemical non-equilibrium

Unstructured grids

ABSTRACT

In this paper we present an extension of Residual Distribution techniques for the simulation of compressible flows in non-equilibrium conditions. The latter are modeled by means of a state-of-the-art multi-species and two-temperature model.

An entropy-based variable transformation that symmetrizes the projected advective Jacobian for such a thermophysical model is introduced. Moreover, the transformed advection Jacobian matrix presents a block diagonal structure, with mass-species and electronic-vibrational energy being completely decoupled from the momentum and total energy sub-system.

The advantageous structure of the transformed advective Jacobian can be exploited by contour-integration-based Residual Distribution techniques: established schemes that operate on dense matrices can be substituted by the same scheme operating on the momentum–energy subsystem matrix and repeated application of scalar scheme to the mass-species and electronic-vibrational energy terms.

Finally, the performance gain of the symmetrizing-variables formulation is quantified on a selection of representative testcases, ranging from subsonic to hypersonic, in inviscid or viscous conditions.

© 2018 Elsevier Inc. All rights reserved.

1. Introduction

Hypersonic flows experience a number of physical phenomena (see e.g. [9]) that become progressively more relevant as the Mach number increases.¹ Among those phenomena, the appearance of strong (possibly detached) shock waves has important implications: the gas crossing such strong shock waves gets highly compressed and intensely heated (i.e. the gas kinetic energy is converted into internal energy). At sufficiently high Mach numbers, the temperature increase in the post-shock region may be enough to induce chemical and thermal non-equilibrium effects, i.e. species dissociation, recombination and/or ionization and excitation of internal molecular energetic modes, phenomena which all need to be considered.

The special characteristics of hypersonic flows set certain constraints on the discretization techniques employed for their numerical resolution. Specifically, a numerical method needs, on the one hand, to be robust enough to handle the strong

* Corresponding author at: E.T.S. Ingeniería Aeronáutica y del Espacio, Universidad Politécnica de Madrid Plaza del Cardenal Cisneros, 3, Madrid, 28040, Spain.

E-mail address: jesus.garicano.mena@upm.es (J. Garicano-Mena).

¹ The conventional threshold distinguishing both regimes is $Ma_\infty \approx 5$.

shock waves (and this in a conservative and monotonicity preserving fashion); on the other hand, the method should be capable of describing accurately the flow gradients across any boundary/shear layer present in the domain. Moreover, accounting for chemical and/or thermal non-equilibrium requires as many additional variables as different chemical species/internal energy modes are considered: the more detailed the non-equilibrium model, the more costly it becomes to achieve a flow solution.

The most standard solvers for hypersonic flow simulation are based on Finite Volume (FV), cell-centered, second-order, shock-capturing schemes working on multi-block, structured grids. Stiffness induced by high cell aspect-ratio and/or non-equilibrium (NEQ) effects is handled by implicit iterative methods, and the resulting linear systems are solved by Krylov subspace methods. LAURA (Langley Aerothermodynamic Upwind Relaxation Algorithm) [27,50] and DPLR (Data-Parallel Line Relaxation) [78] are probably the most renowned research codes representative of this approach.

Accuracy of thermal loads predicted with a structured code is extremely dependent on grid smoothness and alignment with flow features (e.g. shocks, shear waves, jets): generating a suitable mesh often takes more time than running the code itself. Hence the slow, yet progressive shift towards unstructured solvers: complex domains are discretized more easily if one is not constrained to respect a particular grid structure. The highest level of flexibility for meshing is obtained when using exclusively *simplex*² elements. FUN3D (Fully Unstructured Navier–Stokes) [51] and US3D [14] are FV solvers exploiting this new paradigm.

However, obtaining accurate flow predictions on fully tetrahedral meshes is very difficult, due to non-alignment of the shock surface with the grid, which leads to irregularities in the entropy that are convected to the boundary layer. Another reason is that FV methods heavily rely on locally 1D Riemann problems. For simplicial grids, there always exist cell faces in the boundary layer which are oblique to the wall, where these locally 1D Riemann problems lack any physics. One possible solution in the FV context, involving multidimensional upwind reconstruction of the interfacial solution values, has been recently proposed by Gnoffo in [28,29].

Aside of the FV techniques mentioned above, other well-established computational approaches for the transonic aerodynamics field, namely Stabilized Finite Elements (FE) and Discontinuous Galerkin (DG) methods, have been applied to compute hypersonic flow fields.

Kirk and collaborators employ Stabilized FE methods (also known as SUPG schemes): relevant results are shown in references [35] and [34]. Though their method works for general unstructured grids, they mainly report results on Q1 (quadrilateral or hexahedral) elements.

DG schemes have also been applied to hypersonic heating prediction: e.g. Barter and Darmofal [12] employ a shock-capturing framework and perform adaptive, higher-order Discontinuous Galerkin computations on viscous, hypersonic flows around blunt bodies. They also considered an additional scalar advection–diffusion equation to provide the *artificial* viscosity embedded in the shock-capturing term.

Residual Distribution (or RD)³ methods are vertex-centered discretization techniques capable of handling hyperbolic systems of equations on general unstructured simplicial grids.

RD methods present several advantageous features, namely:

- A maximum principle (Local Extrema Diminishing) taken from Finite Volume methods, which allows to capture discontinuities monotonically on general unstructured grids;
- Being based on Finite Element approximation theory, it is possible to obtain, on a compact stencil, 2nd order accurate solutions on unstructured grids, irrespective of the regularity of the mesh;
- A better grid insensitivity on simplicial meshes, thanks to a built-in multidimensional dissipation property, not relying on 1D Riemann solvers.

RD methods have been employed successfully for the discretization and solution of advection–diffusion scalar equations in [63,69,48,49]; and for the compressible Navier–Stokes equations in the context of transonic aerodynamics in references [72,42,7,5],.... In the hypersonic field, the method has been applied to double cone configurations [39] and blunt body problems, both in shock-capturing ([22,23]) and shock fitting ([55,13,59,38]) contexts.

In this contribution, we present a formulation of the inviscid terms that – by exploiting an entropy variables transformation – allows for noticeable computational time reduction. This formulation extends the one presented in reference [20] to the thermal and chemical non-equilibrium case.

The article is organized as follows: section 2 presents the system of equations and the thermo-chemical model describing the flows of our interest. Next, section 3 describes in detail the entropy-variables-based formulation of the governing equations. Section 4 offers then a brief introduction to RD techniques focusing, in particular, on the computation and distribution of convective residuals and how these steps are modified to exploit advantageously the entropy-variables-based formulation. Section 5 presents some recent results obtained with RD on different subsonic and hypersonic non-equilibrium flow configuration; the computational advantage associated to the entropy-variables-based formulation is also demonstrated in section 5. The conclusions are summarized in section 6.

² A *simplex* is a common name for triangles (2D) and tetrahedra (3D).

³ RD techniques are also known under the name of Fluctuation Splitting (FS) schemes[4].

In an attempt to clarify as much as possible the discussion on the entropy-variable-based formulation, all the necessary but non-essential material concerning e.g. details about handling diffusion and source term residuals, imposition of boundary conditions and the solution procedure of the discrete system of nodal equations is gathered in appendix A.

2. Governing equations

In this work we will consider NEQ flows including vibrational excitation and chemical reaction processes, which we will describe by means of a n_S species (with $n_S \geq 2$), two-temperature model [58]. These models assume that translational and rotational contributions to the internal energy are fully excited and in equilibrium at temperature T , while the vibrational and electronic modes are themselves in equilibrium at a temperature T^v possibly different from T . In particular we will employ the equations presented in [26], but restricted to non-ionized mixtures, which are appropriate for the target testcases considered in this paper.

The set of equations describing the flow of a n_S species, electrically neutral gas mixture, possibly reacting and/or under vibrational non-equilibrium conditions is then given by:

$$\begin{aligned} \frac{\partial \rho_s}{\partial t} + \nabla \cdot (\rho_s \tilde{u}) &= \nabla \cdot (-\rho_s \tilde{u}_s^d) + \dot{\omega}_s, \quad s \in \{1, \dots, n_S\} \\ \frac{\partial \rho \tilde{u}}{\partial t} + \nabla \cdot (\rho \tilde{u} \cdot \tilde{u}^t + p \bar{I}_{n_D}) &= \nabla \cdot \bar{\tau}, \\ \frac{\partial \rho E}{\partial t} + \nabla \cdot (\rho H \tilde{u}) &= \nabla \cdot (\bar{\tau} \cdot \tilde{u} - \bar{q}), \\ \frac{\partial \rho e^v}{\partial t} + \nabla \cdot (\rho e^v \tilde{u}) &= \nabla \cdot (-\bar{q}^v) + \Omega^v \end{aligned} \quad (1)$$

together with the appropriate BC's and IC's for the space-time domain $\Omega \times [0, T]$. This system of equations expresses the conservation of mass (at the species level, and globally), momentum and energy (both total and vibrational) principles. In system above, ρ_s stands for the density of the s -th species, while $\rho \tilde{u}$, ρE and ρe^v are respectively the momentum, the total energy and the electronic-vibrational energy per unit volume. Additionally, p is the pressure exerted by the mixture and H is the specific total enthalpy.

Quantity \tilde{u}_s^d stands for the s -th species diffusive velocity, which are obtained from the Stefan–Maxwell equations, as detailed in Ref. [10,75].

The gas mixture behaves as a Newtonian fluid, and hence the viscous stress tensor $\bar{\tau}$, under the hypothesis of negligible bulk viscosity effects, is simply:

$$\tau_{i,j} = \mu \left[\left(\frac{\partial u_j}{\partial x_i} + \frac{\partial u_i}{\partial x_j} \right) - \frac{2}{3} \frac{\partial u_k}{\partial x_k} \delta_{i,j} \right]. \quad (2)$$

The heat flux vector \bar{q} comprises contributions from the gradients of temperature and of vibrational-electronic temperature and from the diffusive transport of energy:

$$q_i = -\lambda \frac{\partial T}{\partial x_i} - \lambda^v \frac{\partial T^v}{\partial x_i} - \sum_s \rho_s h_s u_{s,i}^d. \quad (3)$$

The vibrational heat flux is:

$$q_i^v = -\lambda^v \frac{\partial T^v}{\partial x_i} - \sum_s \rho_s h_s^v u_{s,i}^d. \quad (4)$$

The mass production term for species s is given by the law of mass action:

$$\frac{\dot{\omega}_s}{M_s} = \sum_{\text{reactions}} (v_{s,r}'' - v_{s,r}') \left\{ k_{r,f} \prod_{\text{species}} \left(\frac{\rho_k}{M_k} \right)^{v_{k,r}'} - k_{r,b} \prod_{\text{species}} \left(\frac{\rho_k}{M_k} \right)^{v_{k,r}''} \right\}. \quad (5)$$

Here $k_{r,f}$ and $k_{r,b}$ stand for the forward and backward reaction rates for the r -th reaction; $v_{k,r}'$ and $v_{k,r}''$ are the stoichiometric coefficients and M_k is the molar weight for the k -th species. In this work, the N - N_2 and the 5-species air (Air5) gas mixtures will be employed. The former considers a gas mixture of nitrogen atoms N and molecules N_2 , while the latter assumes non-ionized air composed by atomic nitrogen N and oxygen O , and molecular nitrogen N_2 , oxygen O_2 and nitric oxide NO . Therefore, for a two-dimensional flow computation under thermal and chemical non-equilibrium (TCNEQ), the number of conserved variables is 6 for N – N_2 and 9 for Air5; if only chemical non-equilibrium (CNEQ) is considered, a system of 5 and 8 equations is obtained.

Finally, the term Ω^v , in the case of gas mixtures involving only neutral species (i.e. in absence of ionization) accounts for the energy exchange (relaxation) between translational and vibrational modes and for the energy gained through dissociation or recombination processes:

$$\Omega^v = \sum_{s=1}^{n_S} \rho_s \frac{e_{v,s}^* - e_{v,s}}{\tau_s} + \sum_{s=1}^{n_S} \hat{D}_s \dot{\omega}_s. \quad (6)$$

The model is not closed until initial/boundary conditions, properties D_s , μ , λ , λ^v , $k_{r,f}$, $k_{r,b}$, τ_s and an equation of state are provided.

What are *physically adequate* initial/boundary conditions for the system of non-linear partial differential equations in Eqs. (1) on the space-time domain $\Omega \times [0, T]$ is in itself a complex mathematical problem: the interested reader can refer to [16,30]. Regarding the transport properties, the reader may address references [31] for a detailed account. In this work, we delegate the calculation of all transport, chemistry, thermodynamics and energy transfer properties to the MUTATION library (version 2), described in [56].

At the equation of state level, the ideal gas law for a thermally perfect gas (PG) applies to each of the components of the gas mixture, which exert a *partial* pressure given by $p_s = R \rho_s / M_s T$. Here, R is the universal gas constant $R = 8314.4$ J/K kmol and M_s the s -th species molecular weight (in kg/kmol). The total pressure of the mixture is:

$$p = \sum_{s=1}^{n_S} p_s. \quad (7)$$

Specific enthalpy H relates to pressure as $H = E + p/\rho$. Total energy ρE and pressure p of the mixture can be further related if one realizes that ρE includes contributions from the translational-rotational modes, from the vibrational-electronic modes and from the kinetic energy, as in $\rho E = \rho e^{tr} + \rho e^v + \frac{1}{2} \rho \tilde{u}^t \cdot \tilde{u}$. Each of these gathers in turn contributions from the different species in the mixture:

$$\rho e^{tr} = \sum_{s=1}^{n_S} \rho_s e_s^{tr}, \quad \rho e^v = \sum_{s=1}^{n_S} \rho_s e_s^v, \quad \frac{1}{2} \rho \tilde{u}^t \cdot \tilde{u} = \sum_{s=1}^{n_S} \rho_s \frac{\|\tilde{u}\|^2}{2}.$$

The expression for the s -th species translational-rotational energy e_s^{tr} is:

$$e_s^{tr} = \int_{T^0}^T C_{v,s}^{tr} d\tau + h_s^0, \quad (8)$$

where h_s^0 is the formation enthalpy of the species at the reference temperature T^0 , with $C_{v,s}^{tr}$ the translational-rotational specific heat at constant volume. Since the components of the mixture behave as calorically perfect gases, we have:

$$C_{v,s}^{tr} = \begin{cases} \frac{3}{2} R_s, & \text{for a monatomic species,} \\ \frac{5}{2} R_s, & \text{for a diatomic component.} \end{cases} \quad (9)$$

The expression for the s -th species vibrational energy e_s^v is derived under the assumption that the internal quantum states are populated according to a Boltzmann distribution, so molecular species behave as harmonic oscillators:

$$e_s^v = \begin{cases} 0, & \text{for atomic species,} \\ \frac{R}{M_s} \frac{\theta_s^v}{e^{\theta_s^v/T^v} - 1}, & \text{for diatomic species.} \end{cases} \quad (10)$$

where θ_s^v is a characteristic vibrational temperature for the s -th species.

Differentiating Eq. (7) and algebraic manipulation, see Ref. [45], leads to:

$$dp = \sum_{s=1}^{n_S} \gamma_s d\rho_s + \beta d\rho e^{tr}. \quad (11)$$

Terms γ_s and β in Eq. (11) stand respectively for the partial derivatives of pressure with respect to the translational-rotational energy and the species densities; they are given by:

$$\beta = \frac{\partial p}{\partial \rho e^{tr}} = \frac{\sum_{s=1}^{n_S} \gamma_s R/M_s}{\sum_{s=1}^{n_S} \gamma_s C_{v,s}^{tr}}, \quad \text{and} \quad \gamma_s = \frac{\partial p}{\partial \rho_s} = R/M_s T - \beta e_s^{tr}, \quad (12)$$

where term $\gamma_s \equiv \rho_s/\rho$ is the mass fraction of s -th species. Pressure derivatives γ_s and β intervene as well in the expression for the frozen speed of sound:

$$a^2 = \sum_{s=1}^{n_s} y_s \gamma_s + \left(h - e^v - \frac{\|\vec{u}\|^2}{2} \right) \beta = (1 + \beta) \frac{p}{\rho}. \quad (13)$$

The behavior of gases in CNEQ conditions can be modeled with Eqs. (1) simply by assuming that the vibrational and the roto-translational mode are at equilibrium; this implies that $T^v = T$ and translates into disregarding the conservation equation for the vibrational energy.

In certain conditions, whenever time scales for the microscopic phenomena described so far (chemical reactions, vibrational relaxation) are much longer than the characteristic flow time, those phenomena can be safely neglected. This situation is known as *frozen flow*; it can be modeled simply by nullifying the source terms $\dot{\omega}_s$ and Ω^v .

We now write the physical model described so far in vector form. This compact vector form eases both the description of the RD method in sections 4 and appendix A, and the mathematical derivation leading to the entropy-variable-based formulation considered in sections 3.1 and 3.2.

2.1. Governing equations in compact vector form

The system of advection–diffusion–reaction equations Eqs. (1) can be recast in compact vector form as:

$$\frac{\partial \vec{U}}{\partial t} + \nabla \cdot \vec{\bar{F}}^c = \nabla \cdot \vec{\bar{F}}^d + \vec{S}, \quad (14)$$

where the convective and diffusive tensors are defined as (Einstein convention applies):

$$\vec{\bar{F}}^c = \vec{F}_j^c \cdot \vec{e}_j^t, \quad \vec{\bar{F}}^d = \vec{F}_j^d \cdot \vec{e}_j^t, \quad \text{for } j \in \{x_1, \dots, x_{n_D}\}.$$

and the vectors employed fulfill:

$$\vec{U}, \vec{F}_j^c, \vec{F}_j^d, \vec{S} \in \mathbb{R}^{n_{Eqs}} \text{ and } \{\vec{e}_j\} \text{ is the canonical basis for } \mathbb{R}^{n_D}.$$

Here \vec{U} stands for the vector of conserved variables and tensors $\vec{\bar{F}}^c$ and $\vec{\bar{F}}^d$ collect the convective and diffusive fluxes of the conserved quantities, while vector \vec{S} contains the chemical and internal energy modes source terms.

For a TCNEQ flow, $n_{Eqs} = n_s + n_D + 2$ while $n_{Eqs} = n_s + n_D + 1$ for a CNEQ flow. The vector of conserved variables is:

$$\vec{U} = [\rho_s, \quad \rho u_j, \quad \rho E, \quad \rho e^v]^t, \quad (15)$$

for the TCNEQ case. The components of the convective flux tensor are given by:

$$\vec{F}_j^c = [\rho_s u_j, \quad \rho \vec{u}^t u_j + p \vec{e}_j, \quad \rho H u_j, \quad \rho e^v u_j]^t, \quad j \in \{x_1, \dots, x_{n_D}\}. \quad (16)$$

For the residual distribution discretization employed in this work it is useful to have this system of equations expressed in quasi-linear form, which is obtained by linearizing the advective flux Jacobian:

$$\frac{\partial \vec{U}}{\partial t} + \underbrace{\frac{\partial \vec{F}_j^c}{\partial \vec{U}}}_{A_j^{c,U}} \frac{\partial \vec{U}}{\partial x_j} = \frac{\partial \vec{F}_j^d}{\partial x_j} + \vec{S}, \quad (17)$$

where we have introduced the advective Jacobians $A_j^{c,U} \in \mathbb{R}^{n_{Eqs} \times n_{Eqs}}$. For the gas models considered, the advective Jacobians are such that a matrix κ defined as:

$$\kappa = A_j^{c,U} t_j, \quad \forall t \in \mathbb{R}^{n_D}, \quad (18)$$

has exactly n_{Eqs} real eigenvalues and n_{Eqs} linearly independent eigenvectors. That is equivalent to say that the associated advective system of equations, $\frac{\partial \vec{U}}{\partial t} + \nabla \cdot \vec{\bar{F}}^c = \vec{0}$, is hyperbolic [44,26]. The eigenvalues of κ are:

$$\vec{\lambda}_t = \left[\vec{u} \cdot \vec{t} + a, \underbrace{\vec{u} \cdot \vec{t}, \dots, \vec{u} \cdot \vec{t}}_{n_{Eqs}-2}, \vec{u} \cdot \vec{t} - a \right]^t, \quad (19)$$

where a is the (frozen) speed of sound. Defining the diagonal matrix $\Lambda_t \equiv \text{diag}(\vec{\lambda})$ and arranging the right/left eigenvectors as columns/rows in matrices R_t^U / L_t^U , κ is factored as:

$$\kappa = R_t^U \cdot \Lambda_t \cdot L_t^U. \quad (20)$$

The projected advective Jacobian is [26,45]:

$$A_n^{c,U} = \begin{bmatrix} U_n(\bar{I}_{n_S} - \bar{Y}_{n_S \times 1} \cdot \bar{1}_{1 \times n_S}) & \bar{Y}_{n_S \times 1} \cdot \bar{n}^t & \bar{0}_{n_S \times 1} & \bar{0}_{n_S \times 1} \\ \bar{n} \cdot \bar{\Gamma} - U\bar{u} \cdot \bar{1}_{1 \times n_S} & U\bar{I}_{n_D} + \bar{u} \cdot \bar{n}^t - \beta\bar{n} \cdot \bar{u}^t & \beta\bar{n} & -\beta\bar{n} \\ U_n(\bar{\Gamma} - H \cdot \bar{1}_{1 \times n_S}) & H\bar{n}^t - \beta U_n \bar{u}^t & (1 + \beta)U_n & -\beta U_n \\ -U_n e_v \bar{1}_{1 \times n_S} & e_v \bar{n}^t & 0 & U_n \end{bmatrix}, \quad (21)$$

where $\bar{Y}_{n_S \times 1}$ contains the n_S species mass fractions, $\bar{Y}_{n_S \times 1} = [y_1, \dots, y_{n_S}]^t$. Vector $\bar{\Gamma}_{1 \times n_S}$ accommodates the partial derivatives of pressure with respect to the different species densities, $\bar{\Gamma}_{1 \times n_S} = [\gamma_1, \dots, \gamma_{n_S}]$.

The diffusive flux tensor is:

$$\bar{F}_j^d = \left[-\rho_s u_{s,j}^d, \quad \tau_{i,j}, \quad \tau_{i,j} u_j - q_i, \quad -q_i^v \right]^t, \quad i, j \in \{x_1, \dots, x_{n_D}\}, \quad (22)$$

and the source term \bar{S} is given by:

$$\bar{S} = \left[\dot{\omega}_s, \quad \bar{0}_{1 \times n_D}, \quad 0, \quad \Omega^v \right]^t. \quad (23)$$

The CNEQ case is recovered by just disregarding any e^v related terms. Finally, the flow of an inviscid gas mixture can be described just by neglecting the dissipative processes, that is, by setting term \bar{F}^d to $\bar{0}$.

3. An entropy variables based formulation for the TCNEQ system

In this section, we reformulate the advective term in equation (39) in terms of an entropy variables set; this allows to greatly reduce the operations necessary to distribute the discrete advective residual.

3.1. Symmetrization of conservation laws

For inviscid PG flows, it is possible to decouple one of the equations (namely, the entropy equation) from the system of the Euler equations if an adequate change of variables is performed. In this process the part of the equations that remains coupled can also be symmetrized, see [72].

Degrez and van der Weide extended this idea to inviscid flows in chemical non-equilibrium in [20]. They defined the set of symmetrizing variables given by:

$$\partial \bar{Q} = \left[y_s \partial p - a^2 \partial \rho_s, \quad \partial u_j, \quad \frac{1}{\rho a} \partial p \right]^t, \quad (24)$$

that can be shown to be linked to the species partial entropies. When applied to the Euler equations, all the mass conservation equations get decoupled from the momentum and energy conservation ones. This allowed Degrez and van der Weide to apply scalar RD schemes independently to each of the mass equations while retaining matrix counterparts of the schemes for the reduced momentum–energy subsystem; effectively treating inviscid flows in CNEQ at relatively moderate numerical cost.

As stated in references [15,25], symmetrizability of general conservation laws is assured if an entropy function S exists. In those cases, the linear transformation $\frac{\partial \bar{Q}}{\partial \bar{U}}$ with entropy variables \bar{Q} defined as:

$$\bar{Q}|_m = -\frac{\partial S}{\partial \bar{U}|_m} \quad (25)$$

is guaranteed to recast the complete system of equations in symmetric form.

The symmetric structure obtained through no matter what approach (either that in [15] or [25]) offers already some numerical advantages. However, since in both cases the matrices retrieved are dense, the perspective of obtaining a block structure with scalar independent mass equations makes the extension of Degrez and van der Weide's approach the most appealing option for the n_s -species, two temperature TCNEQ model considered in this work.

3.2. The set of symmetrizing variables

In this section the compact vector formulation described in section 2.1 is employed. In particular, consider the projected advective Jacobian in Eq. (21), computed as the sum of the advective Jacobian for each of the reference directions weighted by the components of a generic unit vector \bar{n} .

$$A_n^{c,U} = \begin{bmatrix} U_n(\bar{\Gamma}_{n_S} - \bar{Y}_{n_S \times 1} \cdot \bar{\Gamma}_{1 \times n_S}) & \bar{Y}_{n_S \times 1} \cdot \bar{n}^t & \bar{0}_{n_S \times 1} & \bar{0}_{n_S \times 1} \\ \bar{n} \cdot \bar{\Gamma} - U\bar{u} \cdot \bar{\Gamma}_{1 \times n_S} & U\bar{I}_{n_D} + \bar{u} \cdot \bar{n}^t - \beta\bar{n} \cdot \bar{u}^t & \beta\bar{n} & -\beta\bar{n} \\ U_n(\bar{\Gamma} - H \cdot \bar{\Gamma}_{1 \times n_S}) & H\bar{n}^t - \beta U_n \bar{u}^t & (1 + \beta)U_n & -\beta U_n \\ -U_n e_v \bar{\Gamma}_{1 \times n_S} & e_v \bar{n}^t & 0 & U_n \end{bmatrix}.$$

In the discussion to follow, matrix $A_n^{c,U}$ will be reexpressed in different sets of variables. The Jacobian matrix $A_n^{c,U}$, in terms of the conservative variables \bar{U} , can be recast in the new set of variables \bar{V} by means of the classical linear algebra relation:

$$A_n^{c,V} = \frac{\partial \bar{V}}{\partial \bar{U}} \cdot A_n^{c,U} \cdot \frac{\partial \bar{U}}{\partial \bar{V}}, \quad (26)$$

where expression $\frac{\partial \bar{U}}{\partial \bar{V}}$ should be interpreted as the matrix whose components are defined as:

$$\left. \frac{\partial \bar{U}}{\partial \bar{V}} \right|_{m,n} = \frac{\partial \bar{U}|_m}{\partial \bar{V}|_n}, \quad m, n \in \{1, \dots, n_{Eqs}\}. \quad (27)$$

Note how Eq. (26) above allows to reexpress the quasi-linear form of the System of Eqs. (17) in the arbitrary variable set \bar{V} while still retaining the vector of conserved variables \bar{U} as the unknown, namely:

$$\frac{\partial \bar{U}}{\partial \bar{V}} \cdot \frac{\partial \bar{V}}{\partial t} + \frac{\partial \bar{U}}{\partial \bar{V}} \cdot A_i^{c,V} \frac{\partial \bar{V}}{\partial x_i} = \nabla \cdot \bar{F}^d + \bar{S}, \quad (28)$$

The first step is to transform the left eigenvectors of matrix $A_n^{c,U}$ to the set of primitive variables $\bar{P} = [\rho_s, u_j, p, e_v]^t$.

The matrix containing the left eigenvectors of $A_n^{c,U}$ is taken from reference [26].⁴ The matrix L^P in primitive variables is obtained from:

$$L^U = \begin{bmatrix} a^2 \bar{\Gamma}_{n_S} - \bar{Y}_{n_S \times 1} \cdot \bar{\Gamma} & \beta \bar{Y}_{n_S \times 1} \cdot \bar{u}^t & -\beta \bar{Y}_{n_S \times 1} & \beta \bar{Y}_{n_S \times 1} \\ -V \bar{\Gamma}_{1 \times n_S} & \bar{l}^t & 0 & 0 \\ -W \bar{\Gamma}_{1 \times n_S} & \bar{m}^t & 0 & 0 \\ \bar{\Gamma} - aU \bar{\Gamma}_{1 \times n_S} & a\bar{n}^t - \beta \bar{u}^t & \beta & -\beta \\ \bar{\Gamma} + aU \bar{\Gamma}_{1 \times n_S} & -a\bar{n}^t - \beta \bar{u}^t & \beta & -\beta \\ -e_v \bar{\Gamma} & \beta e_v \bar{u}^t & -\beta e_v & a^2 + \beta e_v \end{bmatrix}, \quad (29)$$

through the relationship $L^P = L^U \cdot \frac{\partial \bar{U}}{\partial \bar{P}}$, leading eventually to:

$$L^P = \begin{bmatrix} a^2 \bar{\Gamma}_{n_S} & 0_{n_S \times 3} & -\bar{Y}_{n_S \times 1} & \bar{0}_{n_S \times 1} \\ \bar{0}_{1 \times n_S} & \rho \bar{l}^t & 0 & 0 \\ \bar{0}_{1 \times n_S} & \rho \bar{m}^t & 0 & 0 \\ \bar{0}_{1 \times n_S} & a\bar{n}^t & 1 & 0 \\ \bar{0}_{1 \times n_S} & -a\bar{n}^t & 1 & 0 \\ a^2 e_v \bar{\Gamma}_{1 \times n_S} & \bar{0}_{1 \times n_D} & -e_v & \rho a^2 \end{bmatrix}. \quad (30)$$

Inspecting then the first (block) row of matrix L^P , one recognizes the combination of variables that decouples the mass related terms from the rest: it is the same as for the CNEQ case (compare with Eq. (24)). Further inspection suggests the possibility of decoupling also the terms related with the vibrational energy. The following definition for the symmetrizing variables is considered:

$$\partial \bar{Q} = \left[y_s \partial p - a^2 \partial \rho_s, \quad \partial u_i, \quad \frac{\partial p}{\rho a}, \quad \frac{e_v}{\rho} \partial p - \frac{a^2 e_v}{\rho} \sum_s \partial \rho_s - a^2 \partial e_v \right]^t. \quad (31)$$

The transformation matrices between the conservative and the symmetrizing sets of variables for thermal and chemical non-equilibrium are:

⁴ The definition used here is inverse of the one used in the original reference [26].

$$\frac{\partial \vec{Q}}{\partial \vec{U}} = \begin{bmatrix} \vec{Y}_{n_S \times 1} \cdot \vec{\Gamma} - a^2 \vec{I}_{n_S} & -\beta \vec{Y}_{n_S \times 1} \vec{u}^t & \beta \vec{Y}_{n_S \times 1} & -\beta \vec{Y}_{n_S \times 1} \\ -\frac{\vec{u}}{\rho} \cdot \vec{1}_{1 \times n_S} & \frac{1}{\rho} I_3 & \vec{0}_{3 \times 1} & \vec{0}_{n_D \times 1} \\ \frac{\vec{\Gamma}}{\rho a} & -\frac{\beta \vec{u}^t}{\rho a} & \frac{\beta}{\rho a} & -\frac{\beta}{\rho a} \\ \frac{e_v}{\rho} \vec{\Gamma} & -\frac{\beta e_v}{\rho} \vec{u}^t & \frac{\beta e_v}{\rho} & \frac{1}{\rho} (-\beta e_v - a^2) \end{bmatrix}, \quad (32)$$

and:

$$\frac{\partial \vec{U}}{\partial \vec{Q}} = \begin{bmatrix} -\frac{1}{a^2} \vec{I}_{n_S} & \vec{0}_{n_S \times n_D} & \frac{\rho}{a} \vec{Y}_{n_S \times 1} & \vec{0}_{n_S \times 1} \\ -\frac{1}{a^2} \vec{u} \cdot \vec{1}_{1 \times n_S} & \rho I_3 & \frac{\rho}{a} \vec{u} & \vec{0}_{n_D \times 1} \\ \frac{\vec{\Gamma}}{\beta a^2} - \frac{v^2}{a^2} \vec{1}_{1 \times n_S} & \rho \vec{u}^t & \rho \frac{H}{a} & -\frac{\rho}{a^2} \\ \vec{0}_{1 \times n_S} & \vec{0}_{1 \times n_D} & \frac{\rho e_v}{a} & -\frac{\rho}{a^2} \end{bmatrix}. \quad (33)$$

With these matrices, the advective Jacobian in terms of symmetrizing variables is calculated simply as:

$$A_n^{c,Q} = \frac{\partial \vec{Q}}{\partial \vec{U}} \cdot A_n^{c,U} \cdot \frac{\partial \vec{U}}{\partial \vec{Q}} = \begin{bmatrix} U_n \vec{I}_{n_S} & \vec{0}_{n_S \times n_D} & \vec{0}_{n_S \times 1} & \vec{0}_{n_S \times 1} \\ \vec{0}_{n_D \times n_S} & U_n \vec{I}_{n_D} & a \vec{n} & \vec{0}_{n_D \times 1} \\ \vec{0}_{1 \times n_S} & a \vec{n}^t & U_n & 0 \\ \vec{0}_{1 \times n_S} & \vec{0}_{1 \times n_D} & 0 & U_n \end{bmatrix} \quad (34)$$

where decoupling of mass terms and vibrational energy is evident. However, and for reasons to be discussed in section 4, one needs to compute as well the eigenvectors in the new symmetrizing variables Q .

Left and right eigenvectors matrices in symmetrizing variables are computed from those expressed in conservative variables, taken again from [26]. The matrix whose rows are the left eigenvectors in Q variables is:

$$L^Q = L^U \cdot \frac{\partial \vec{U}}{\partial \vec{Q}} = \begin{bmatrix} -\vec{I}_{n_S} & \vec{0}_{n_S \times n_D} & \vec{0}_{n_S \times 1} & \vec{0}_{n_S \times 1} \\ \vec{0}_{1 \times n_S} & \rho \vec{l}^t & 0 & 0 \\ \vec{0}_{1 \times n_S} & \rho \vec{m}^t & 0 & 0 \\ \vec{0}_{1 \times n_S} & \rho a \vec{n}^t & \rho a & 0 \\ \vec{0}_{1 \times n_S} & -\rho a \vec{n}^t & \rho a & 0 \\ \vec{0}_{1 \times n_S} & \vec{0}_{1 \times n_D} & 0 & -\rho \end{bmatrix}. \quad (35)$$

Conversely, the right eigenvectors matrix is:

$$R^Q = \frac{\partial \vec{Q}}{\partial \vec{U}} \cdot R^U = \begin{bmatrix} -\vec{I}_{n_S} & \vec{0}_{n_S \times 1} & \vec{0}_{n_S \times 1} & \vec{0}_{n_S \times 1} & \vec{0}_{n_S \times 1} & \vec{0}_{n_S \times 1} \\ \vec{0}_{n_D \times n_S} & \frac{1}{\rho} \vec{l} & \frac{1}{\rho} \vec{m} & \frac{1}{2\rho a} \vec{n} & -\frac{1}{2\rho a} \vec{n} & \vec{0}_{3 \times 1} \\ \vec{0}_{1 \times n_S} & 0 & 0 & \frac{1}{2\rho a} & \frac{1}{2\rho a} & 0 \\ \vec{0}_{1 \times n_S} & 0 & 0 & 0 & 0 & -\frac{1}{\rho} \end{bmatrix}. \quad (36)$$

Observe how the particular structure of the transformed Jacobian $A_n^{c,Q}$ in Eq. (34) implies that, at least for the advective contributions, the original $n_S + n_D + 2$ system reduces to $n_S + 1$ independent scalar equations and a $n_D + 1$ subsystem. This point is made explicit by using Equations (31) and (34) to write the transformed inviscid, non-reactive system of equations:

$$\begin{aligned} y_s \frac{\partial p}{\partial t} - a^2 \frac{\partial \rho_s}{\partial t} + y_s \vec{u} \cdot \nabla p - a^2 \vec{u} \cdot \nabla \rho_s &= 0, \\ \frac{\partial u_i}{\partial t} + \vec{u} \cdot \nabla u_i + a \frac{1}{\rho a} \nabla p &= 0, \\ \frac{1}{\rho a} \frac{\partial p}{\partial t} + a \nabla \cdot \vec{u} + \frac{1}{\rho a} \vec{u} \cdot \nabla p &= 0, \\ \frac{e_v}{\rho} \frac{\partial p}{\partial t} - \frac{a^2 e_v}{\rho} \sum_s \frac{\partial \rho_s}{\partial t} - a^2 \frac{\partial e_v}{\partial t} + \\ \frac{e_v}{\rho} \vec{u} \cdot \nabla p - \frac{a^2 e_v}{\rho} \vec{u} \cdot \sum_s \nabla \rho_s - a^2 \vec{u} \cdot \nabla e_v &= 0. \end{aligned} \quad (37)$$

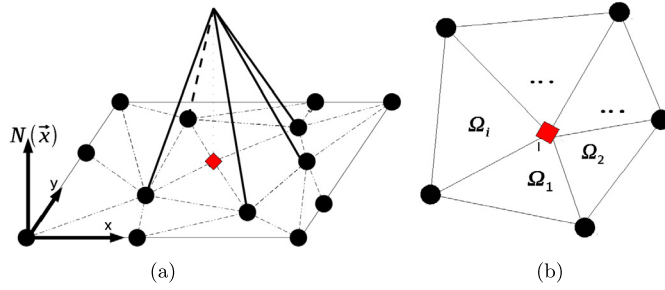


Fig. 1. Discretization in RDS: (a), P_1 nodal basis function for l -th node; (b), set Ξ_l of elements surrounding l -th node.

Note that System (37) is not expressed in conservative form. A recent contribution [8] describes a strategy to handle system of equations in non-conservation form. In this work, however, we will not apply directly *RD* techniques to discretize System (37). In the next section, after a brief presentation on the *RD* discretization, we will describe an strategy that, while solving System (1), exploits advantageously the entropy-variables-based formulation to decrease the computational cost of *TCNEQ* flow simulations.

4. Residual distribution techniques

In this section, we briefly introduce the *RD* discretization for the system of equations (1) by reviewing the main concepts from references [72,62].

Assume we intend to solve Equation (1) on a simplicial tessellation Ω^h of the spatial domain Ω . Let us denote by n_{Elem} and n_{DoF} the number of *simplices* (triangles in 2D, tetrahedra in 3D) and vertices in Ω^h . The numerical solution to Eq. (14), \tilde{U}^h can be immediately expanded in terms of the associated nodal basis functions $N_j \in P^1(\Omega^h)$, see Fig. 1a:

$$\tilde{U}^h(\vec{x}, t) = \sum_{j=1}^{n_{DoF}} \tilde{U}_j(t) N_j(\vec{x}) \quad (38)$$

where the nodal basis functions N_j fulfill $N_j(\vec{x}_k) = \delta_{jk}$.

The steady state residual for element Ω_i is defined as:

$$\vec{\Phi}^{\Omega_i} = \int_{\Omega_i} \left(\frac{\partial \vec{F}_j^c}{\partial x_j} - \frac{\partial \vec{F}_j^d}{\partial x_j} - \vec{S} \right) dv = \vec{\Phi}^{c, \Omega_i} - \vec{\Phi}^{d, \Omega_i} - \vec{\Phi}^{S, \Omega_i}, \quad (39)$$

and gathers contributions from the convective, dissipative and source terms.

An equation for each of the nodal *DoF*'s is obtained by distributing fractions of the cell residuals $\vec{\Phi}^{\Omega_i}$ to the nodes forming part of the cell; in this manner, the l -th *DoF* collects contributions from all the elements in region Ξ_l (see Fig. 1b):

$$\vec{\Phi}_l = \sum_{\Omega_i \in \Xi_l} \vec{\Phi}_l^{\Omega_i} = \sum_{\Omega_i \in \Xi_l} \left(\mathcal{f}^c(\vec{\Phi}^{c, \Omega_i}) + \mathcal{f}^d(\vec{\Phi}^{d, \Omega_i}) + \mathcal{f}^S(\vec{\Phi}^{S, \Omega_i}) \right). \quad (40)$$

Different choices for the functionals $\mathcal{f}^c, \mathcal{f}^d, \mathcal{f}^S$ in Eq. (40) define the different schemes employed. In this section we will concentrate on the computation and distribution of the convective residuals, deferring the diffusive, source term and boundary conditions (BC) contributions, together with the solution strategy to Appendix A.

4.1. Convective residual

The convective contribution to the nodal equation of the cell residual is expressed generically as:

$$\vec{\Phi}_l^c = \sum_{\Omega_i \in \Xi_l} B_l^{\Omega_i} \cdot \vec{\Phi}^{c, \Omega_i}, \quad (41)$$

in terms of the so called distribution matrices $B_l^{\Omega_i}$.

RD schemes can be classified according to how the convective residual is computed: we distinguish among linearization-based (*LRD*) and contour-integration-based (*CRD*) schemes. This distinction is the subject of the next section.

⁵ Superscript h marks here the solution obtained as a numerical approximation. Unless we want to insist on this fact, we will often drop the superscript.

4.1.1. Computing the advective residual: LRD vs CRD

Certain thermodynamic models allow to simultaneously express both the conserved variables vector \vec{U} and the flux vector components \vec{F}_j as a polynomial of at most 2nd degree in the components of a certain vector \vec{Z} . Whenever such vector \vec{Z} exists, one can linearize simultaneously both \vec{U} and \vec{F}_j , greatly simplifying the implementation of approximate Riemann solvers.

For the perfect gas model, such a linearization is available: the Roe linearization introduced in [65], developed originally for dimensionally split FV methods. Later on, Deconinck et al. extended the linearization procedure to the multi-dimensional RD framework, [18]. This breakthrough spawned a number of *linearization-based* residual distribution (LRD) schemes, see [73, 3,4].

Unfortunately, for the NEQ models considered in this work, a \vec{Z} variable is not readily available. Degrez and van der Weide, building upon Liu and Vinokur's ideas [45], proposed a linearization procedure circumventing this limitation in [20]. The merits and shortcomings of this approach are discussed elsewhere, see [22].

There is yet another alternative approach whenever a \vec{Z} variable cannot be defined: the element residual evaluation $\vec{\Phi}^{c,\Omega_i}$ and its distribution can be done independently (see [17,70]) as long as $\vec{\Phi}^{c,\Omega_i}$ respects second equality in flux conservation (see Eq. (43) further ahead) and the distribution coefficients employed respect the consistency condition:

$$\sum_{l \in \Omega_i} B_l^{\Omega_i} = \vec{I}_{nEqS}. \quad (42)$$

Residual Distribution reformulations exploiting this approach are termed *Contour-Integration* (CRD, [17,62]) or *Flux Quadrature* (FQ-RD, [70]) schemes.

As for the actual evaluation of the element residual, it is enough that integral:

$$\vec{\Phi}^{c,\Omega_i} = \int_{\Omega_i} \nabla \cdot \vec{F}_j dv = \oint_{\delta\Omega_i} \vec{F}_j \vec{n}_j^{ext} ds, \quad (43)$$

is evaluated with an error lower than the distribution error, [3,77]. In this work we follow the approach in [17] and evaluate the contour integral by numerical (Gauss) integration:

$$\vec{\Phi}^{c,\Omega_i} = \oint_{\delta\Omega_i} \vec{F}_j \vec{n}_j^{ext} ds = \sum_{f=1}^{n_D+1} \int_{S_f} \vec{F}_j \vec{n}_j^{ext} ds = \sum_{f=1}^{n_D+1} \sum_{q \in Q^P} \omega_q \left(\vec{F}_j \vec{n}_j^{ext} \right)_q l_q, \quad (44)$$

where the sum indexed by q extends over the quadrature points on each of the element faces (edges in 2D). For the specific case considered in this work, namely when expanding the solution in $P1$ basis functions on 2D simplex elements, a two-point quadrature rule is enough, i.e. $Q^P = 2$, see [3,77].

The actual integration is accomplished by mapping each edge to the line $\chi \in [-1, 1]$; the quadrature points are $\chi_{1,2} = \pm 0.577350269189626$ and the corresponding weights $\omega_{1,2} = 1$, see [61].

4.1.2. Distributing the advective residual: matrix RD schemes

The convective contribution to the nodal equation of the cell residual (namely, the distributive functional f^c) in Eq. (40) is expressed generically as:

$$\vec{\Phi}_l^c = \sum_{\Omega_i \in \Xi_l} B_l^{\Omega_i} (K^\pm) \cdot \vec{\Phi}^{c,\Omega_i}. \quad (45)$$

Distribution matrices $B_l^{\Omega_i}$ depend in turn on the nodal upwind parameters K_j , given by:

$$K_k = \frac{1}{n_D} A_{x_d}^{c,U} n_{x_d,k}, \text{ and } k \in \{1, \dots, n_D + 1\}, \quad (46)$$

Hyperbolicity of the Euler subsystem guarantees that these can be factorized as (see section 2.1):

$$K_k = \frac{1}{n_D} A_{x_d}^{c,U} n_{x_d,k} = \frac{1}{n_D} R_k^U \cdot \Lambda_k \cdot L_k^U, \quad (47)$$

where Λ_k is the diagonal matrix containing the eigenvalues in Eq. (19), and R_k^U/L_k^U are matrices whose columns/rows are the right/left eigenvectors of K_k . Splitting the positive and negative parts of Λ_l as Λ_l^+/Λ_l^- , we finally obtain:

$$K_l^\pm = \frac{1}{n_D} R_l^U \cdot \Lambda_l^\pm \cdot L_l^U. \quad (48)$$

Matrix $|K_l|$ is then defined:

$$|K_l| = K_l^+ - K_l^- = \frac{1}{n_D} R_l^U \cdot (\Lambda_l^+ - \Lambda_l^-) \cdot L_l^U, \quad (49)$$

Regarding CRD schemes, whichever inconsistent average state $\bar{V}_{avg,*}$ could be employed to define the upwind K_l and the distribution matrices $B_l^{\Omega_i}$. Throughout this work, we have employed the arithmetic average of the conserved variables $\bar{U}_{avg} = \frac{1}{n_D+1} \sum_{k=1}^{n_D+1} \bar{U}_k$.

We present now several RD schemes and discuss their properties.

Low diffusion A scheme

Introduced originally in [71], Van der Weide and collaborators derived the distribution matrix for system of equations in [74,72]. The CRD variant of the scheme is [62]:

$$B_l^{\Omega_i, LDAc} = K_l^+ \cdot \left(\sum_j K_j^+ \right)^{-1}. \quad (50)$$

This scheme is linear, preserves linear solutions (i.e. is 2nd order accurate) and is multidimensional upwind. It is probably the most used RD scheme for the simulation of smooth flow fields.

Narrow scheme

We describe here the Nc scheme as done originally in [17], by introducing first the $LRD N$ scheme.

The scalar N was devised by Roe in [64], and reformulated as a matrix RD scheme by van der Weide in [73,72]. The N scheme contribution to the nodal residual is given by:

$$\bar{\Phi}_l^{c, \Omega_i, N} = K_l^+ \cdot (\bar{U}_l - \bar{U}_{inlet}^{\Omega_i}), \quad (51)$$

where the *inlet* state $\bar{U}_{inlet}^{\Omega_i}$ reads:

$$\bar{U}_{inlet}^{\Omega_i} = \left(\sum_{j \in \Omega_i} K_j^- \right)^{-1} \cdot \sum_{j \in \Omega_i} K_j^- \cdot \bar{U}_j. \quad (52)$$

The N scheme is linear, multi-dimensional upwind and *positive*; hence it is only 1st order accurate, in agreement with Godunov's theorem. Note that a distribution matrix cannot be obtained explicitly for the system N scheme.

There is an important relationship between the N and the LDA schemes, namely that N scheme is precisely the LDA scheme supplemented by an additional dissipative term $\bar{\delta}_l^{Diss, N}$ of crosswind nature [17,62]:

$$\bar{\Phi}_l^{c, \Omega_i, N} = \bar{\Phi}_l^{c, \Omega_i, LDA} + \bar{\delta}_l^{Diss, N}. \quad (53)$$

Concerning the CRD variant, the Nc scheme is given by:

$$\bar{\Phi}_l^{c, \Omega_i, Nc} = \bar{\Phi}_{l,*}^{c, \Omega_i, N} - B_l^{\Omega_i, LDA} \delta \bar{\Phi}^c, \quad (54)$$

where $\bar{\Phi}_{l,*}^{c, \Omega_i, N}$ is the result of the inconsistent evaluation of Eq. (51) and $\delta \bar{\Phi}^c$ is the difference between the inconsistent element residual $\bar{\Phi}_{\Omega,*}^c|_{Inconsistent}$ and the residual given by Eq. (44):

$$\delta \bar{\Phi}^c = \bar{\Phi}_{\Omega,*}^c|_{Inconsistent} - \bar{\Phi}_{\Omega}^c|_{Gauss}, \quad (55)$$

where the inconsistent element residual $\bar{\Phi}_{\Omega,*}^c|_{Inconsistent}$ is computed as:

$$\bar{\Phi}_{\Omega,*}^c|_{Inconsistent} = \sum_{k \in \Omega_i} K_k \bar{U}_k. \quad (56)$$

Relation (53) holds for the Nc - $LDAc$ pair as well. There is, nevertheless, an important difference between the original N scheme and its CRD variant: the Nc scheme is non-positive [17], meaning that the capture of certain shock waves may present oscillations. This is not a concern for PG simulations, as long as one uses the Roe–Struijs–Deconinck linearization variable \bar{Z} , (in that case Nc and N schemes coincide). The lack of monotonicity is, however, specially problematic for NEQ flows whenever strong, bow shock waves are present in the domain (i.e. precisely when \bar{Z} variable is less likely to be well-defined, see [22]). The underlying reason is the mass production terms – Eq. (5) – highly non-linear dependence

on temperature: the extreme variations in temperature across the numerically captured shock wave result in unphysical production/destruction of species, and this leads eventually to simulation breakdown [24,22]. We defer the description of a strategy to handle such situations to the introduction of the Blended schemes.

Blended schemes

As we did for the Nc - N pair, we start by introducing first the LRD version of the B scheme and deriving from that its CRD counterpart, the Bc scheme.

A family of non-linear schemes can be obtained from a weighted averaging of N and LDA schemes:

$$\vec{\Phi}_l^{c,\Omega_i,B} = \Theta^{\Omega_i} \vec{\Phi}_l^{c,\Omega_i,N} + \left(\bar{I}_{nEqS} - \Theta^{\Omega_i} \right) \vec{\Phi}_l^{c,\Omega_i,LDA}, \quad (57)$$

The resulting scheme is therefore multi-dimensional upwind, positive and linearity preserving. Many variants can be constructed [72,3,69,21,24,49] depending on the choice of Θ^{Ω_i} . Here, we will use the shock detector functions described in Dobeš et al. [21] and in Garicano-Mena et al. [24]. Both of them define Θ^{Ω_i} as the identity matrix times a scalar shock sensor θ , as:

$$\Theta^{\Omega_i} = \theta \bar{I}_{nEqS}. \quad (58)$$

- Dobeš et al. [21], in their Bx scheme, choose a scalar shock sensor θ that depends on the gradient of one of the field variables (pressure, temperature or density), and requires tuning a parameter related to the shock intensity.
- Garicano-Mena et al. [24] adapt the shock sensor in Ref. [29] to the RD context. This detector is parameter-free and works optimally for strong, detached bow shock problems.

Relation (53), when substituted into equation (57) leads to:

$$\vec{\Phi}_l^{c,\Omega_i,B} = \vec{\Phi}_l^{c,\Omega_i,LDA} + \theta \vec{\delta}_l^{Diss,N}. \quad (59)$$

This expression is conceptually akin to *stabilized* finite element schemes [32,33]: the first term takes care of advection of smooth information while the second term, locally active (*i.e.* modulated by the shock detector), provides additional dissipation to handle strong gradients.

Concerning the CRD Bc scheme actually used in this work, the term $\vec{\delta}_l^{Diss,Nc}$ is – as we stated before – non-positive, and hence oscillations across the shock wave may appear for NEQ flows. A straightforward strategy to attenuate these oscillations is simply to supplement the cross-wind term $\vec{\delta}_l^{Diss,Nc}$ with additional dissipation, as in:

$$\vec{\Phi}_l^{c,\Omega_i,Bc} = \vec{\Phi}_l^{c,\Omega_i,LDAc} + \theta \left(\vec{\delta}_l^{Diss,Nc} + \vec{\delta}_l^{Diss,D} \right). \quad (60)$$

The supplementary dissipative term $\vec{\delta}_l^{Diss,D}$ is, of course, modulated also by the shock detector θ .

In this work we employ as additional dissipation term $\vec{\delta}_l^{Diss,D}$ that of the simple Lax–Friedrichs (or Rusanov) scheme [43, 66]. This term can be recast in RD form as (see [4]):

$$\vec{\delta}_l^{Diss,LxF} = \max_{k \in \Omega_i} |\lambda_k| \sum_{m \in \Omega_i} \left(\vec{U}_l - \vec{U}_m \right), \quad (61)$$

where λ_k are the eigenvalues of K_l . Alternatively, other, possibly more complex dissipative terms could be employed: guidelines to design physically based shock-capturing terms $\vec{\delta}_l^{Diss,D}$ are provided in [23].

4.1.3. CRD advective residual distribution in symmetrizing-variables

At the sight of the different CRD schemes presented in section 4.1.2, note how the most computationally intensive operation is always the inversion of matrix factors given by $\left(\sum_j K_j^\pm \right)$.

Observe then the advantageous structure of matrices in Eqs. (34), (35) and (36). Specifically, decoupling of mass and vibrational terms from the momentum–energy part is evident in Eq. (34). If the distribution of the advective residual was performed in terms of the symmetrizing variables \vec{Q} , then the application of Eqs. (50), (54) and (60) would be greatly simplified.

It is indeed possible to distribute the advective residual in terms of the \vec{Q} variable set, by resorting to Eq. (28) (see *e.g.* in [2]). Taking into account only advective contributions, the nodal update is reexpressed as:

$$\vec{\Phi}_l^c = \sum_{\Omega_i \in \Xi_l} \frac{\partial \vec{U}}{\partial \vec{Q}} \cdot B_l^{c,\Omega_i} \cdot \vec{\Phi}_l^{c,\Omega_i}, \quad (62)$$

where the only change with respect to Eq. (41) lies in computing matrices B_l^{c, Ω_i} in terms of upwind parameters defined not in terms of the Jacobians in conserved-variables $A_n^{c, U}$ but in terms of the symmetrizing variables $A_n^{c, Q}$. In virtue of Eq. (47) this translates into defining the upwind parameters as:

$$K_k^Q = \frac{1}{n_D} R_k^Q \cdot \Lambda_k \cdot L_k^Q. \quad (63)$$

The upwind parameter matrices K_k^Q above inherit the special structure imposed by Eq. (34). This implies that the advective residual distribution can be accomplished by applying separately $n_S + 1$ times a scalar *RD* scheme to distribute the vibrational energy and all the mass related residuals while keeping a system scheme for the reduced, $(n_D + 1) \times (n_D + 1)$ momentum-total energy subsystem (i.e. 3×3 for a 2D and 4×4 for 3D simulation). This compares advantageously with the original formulation in conserved variables, formulated in terms of dense $n_S + n_D + 2$ matrices. The reduction on the size of the matrices involved in the element-to-node distribution process suggests that a decrease in the computational effort should be observed. That is the case indeed, as we will show in section 5.4.

Distribution of the decoupled mass and vibrational energy related contributions are performed with the scalar counterparts of the system *RD* schemes presented in section 4.1.2 above. By substituting the system upwind parameters K_j by its scalar counterparts k_j , the scalar schemes are immediately retrieved. More specifically, if one knows e.g. the system expression of the *LDAC* scheme (Eq. (50)), then its scalar version is immediately retrieved as:

$$b_l^{\Omega_i, LDAC} = \frac{k_l^+}{\sum_j k_j^+}, \quad (64)$$

where k_j^+ are computed as:

$$k_j^+ = \frac{1}{n_D} \max(\vec{u} \cdot \vec{n}_j, 0), \quad (65)$$

which can be compared to Eq. (47).

The hybrid system-scalar distribution matrix for the *LDAC* scheme would then be:

$$B_l^{\Omega_i, LDAC-Hybrid} = \begin{bmatrix} b_l^{\Omega_i, LDAC} \bar{I}_{n_S} & \vec{0}_{n_S \times (n_D+1)} & \vec{0}_{n_S \times 1} \\ \vec{0}_{(n_D+1) \times n_S} & M_{(n_D+1) \times (n_D+1)} & \vec{0}_{(n_D+1) \times 1} \\ \vec{0}_{1 \times n_S} & \vec{0}_{1 \times n_S} & b_l^{\Omega_i, LDAC} \end{bmatrix}. \quad (66)$$

System related submatrix $M_{(n_D+1) \times (n_D+1)}$ is given by:

$$M_{(n_D+1) \times (n_D+1)} = K_l^{Q,+}(I_{min} : I_{max}, J_{min} : J_{max}) \cdot \left(\sum_j K_j^{Q,+}(I_{min} : I_{max}, J_{min} : J_{max}) \right)^{-1}, \quad (67)$$

where *fortran*-like indexing in relation to Eq. (63) has been used. The indexes are $I_{min} = J_{min} = n_S + 1$ and $I_{max} = J_{max} = n_S + n_D + 1$.

The expression for the nodal update in Eq. (62) allows to derive an estimate of cost decrease when the distribution is performed in symmetrizing variables. We provide such estimate for the *LDAC* scheme, though the line of reasoning followed here applies to the other schemes considered in this work.

Equation (62) is equivalent to Eq. (82) (or to the assembled Eq. (40), particularized the frozen inviscid case) but accounts explicitly for the possibility of distributing the convective residual in a variable set \bar{Q} different from the conserved variable set \bar{U} .

Computing the *LDAC* element-to-node contribution requires matrix multiplying $B_l^{\Omega_i, LDAC}$ with cell residual $\vec{\Phi}^{c, \Omega_i}$. Since the system of equations we work with involves $n_{Eq} = n_S + n_D + 2$ variables, distributing the residual with the standard conserved-variables-formulation requires:

1. Two matrix sums, involving $\mathcal{O}(n_{Eq}^2)$ flops each,
2. A matrix inversion, involving $\mathcal{O}(n_{Eq}^4)$ flops,
3. Two matrix-matrix products, involving $\mathcal{O}(n_{Eq}^3)$ flops each.

The $\mathcal{O}(n_{Eq}^4)$ inversion operation is the most costly step of the distribution procedure in conserved variables \bar{U} .

Table 1Hypersonic inviscid TCNEQ flow around cylinder. $N - N_2$ mixture. Testcase definition.

Ma_∞	ρ_∞ [kg/m ³]	u_∞ [m/s]	T_∞ [K]	$T_{v,\infty}$ [K]
6.2	5.1512×10^{-3}	5590.	1833.	1833.
Composition				
$y_{N,\infty}$ [–]		$y_{N_2,\infty}$ [–]		
0.9621		0.0379		

Table 2

Hypersonic inviscid TCNEQ flow around cylinder. Air5 mixture. Testcase definition.

Ma_∞	ρ_∞ [kg/m ³]	u_∞ [Pa]	T_∞ [K]	$T_{v,\infty}$ [K]
6.5	5.1512×10^{-3}	5590.	1833.	1833.
Composition				
$y_{N,\infty}$ [–]	$y_{O,\infty}$ [–]	$y_{N_2,\infty}$ [–]	$y_{NO,\infty}$ [–]	$y_{O_2,\infty}$ [–]
0.	0.	0.767	0.	0.233

Alternatively, when the entropy-variables-based formulation is employed, the effort to distribute the residual is given as:

1. On the $n_D + 1$ mass-total energy subsystem:
 - 1.1 Two matrix sums, involving $\mathcal{O}((n_D + 1)^2)$ flops each,
 - 1.2 A matrix inversion, involving $\mathcal{O}((n_D + 1)^4)$ flops,
 - 1.3 Two matrix-matrix products, involving $\mathcal{O}((n_D + 1)^3)$ flops each.
2. For each of the $n_S + 1$ entropy-related variables:
 - 2.1 Two scalar sums, 2 flops,
 - 2.2 A division, 1 flop,
 - 2.3 Two scalar-scalar multiplications, 2 flops,
3. A matrix product (to transform back the residual to conserved variables), involving $\mathcal{O}(n_{Eq}^3)$ flops.

One might be tempted to say that the performance of the entropy-variables-based formulation is controlled by the final matrix-product transforming the element-to-node contributions from the \tilde{Q} to the \tilde{U} variables, involving $\mathcal{O}(n_{Eq}^3)$ flops. However, since matrix $\frac{\partial \tilde{U}}{\partial Q}$ is known analytically (Eq. (33)), the cost can be reduced by block-subdividing vector $B_l^{c,\Omega_i} \cdot \tilde{\Phi}^{c,\Omega_i}$ and exploiting the particular structure of $\frac{\partial \tilde{U}}{\partial Q}$ in the code.

5. Results

In this section three non-equilibrium flow testcases are presented. The corresponding flow fields have been computed with the open source COOLFLUID solver [1,40], that implements the thermophysical model and the Residual Distribution schemes as described in sections 2, 4 and appendix A.

The selected testcases include inviscid and viscous flow fields in both the subsonic and hypersonic regimes, and account for chemical and thermal non-equilibrium effects. The inviscid hypersonic flow around a cylinder is considered in section 5.1. Next, the Air5 viscous subsonic flow around a cylinder is discussed in section 5.2. Then, the $N-N_2$ viscous hypersonic flow around a double cone configuration is the subject of section 5.3.

Finally, section 5.4 presents a study of the performance improvement observed when the symmetrizing variables formulation is applied to the three testcases described before.

5.1. Inviscid TCNEQ hypersonic flow around cylinder

In this section we consider the inviscid flow around the mid-section of a circular cylinder (25.4 mm in radius) placed into a hypersonic stream in TCNEQ conditions. Two different gas mixtures have been considered, $N-N_2$ and Air5; the specific conditions considered are presented in Tables 1 and 2, respectively.

The results presented in this section have been obtained with the Bcx scheme in (60), employing the additional shock dissipation in Eq. (61) and the shock detector from [29,24]. Flow tangency (inviscid wall BC) has been imposed at the wall, a supersonic inlet at the inflow curved boundary and supersonic outlet at the remaining boundaries. The solutions have been obtained in triangular meshes of resolution $n_T \times n_R = 242 \times 129$ nodes, i.e. with $n_{Elem} = 6.1 \times 10^4$ and $n_{Dof} = 3.1 \times 10^4$

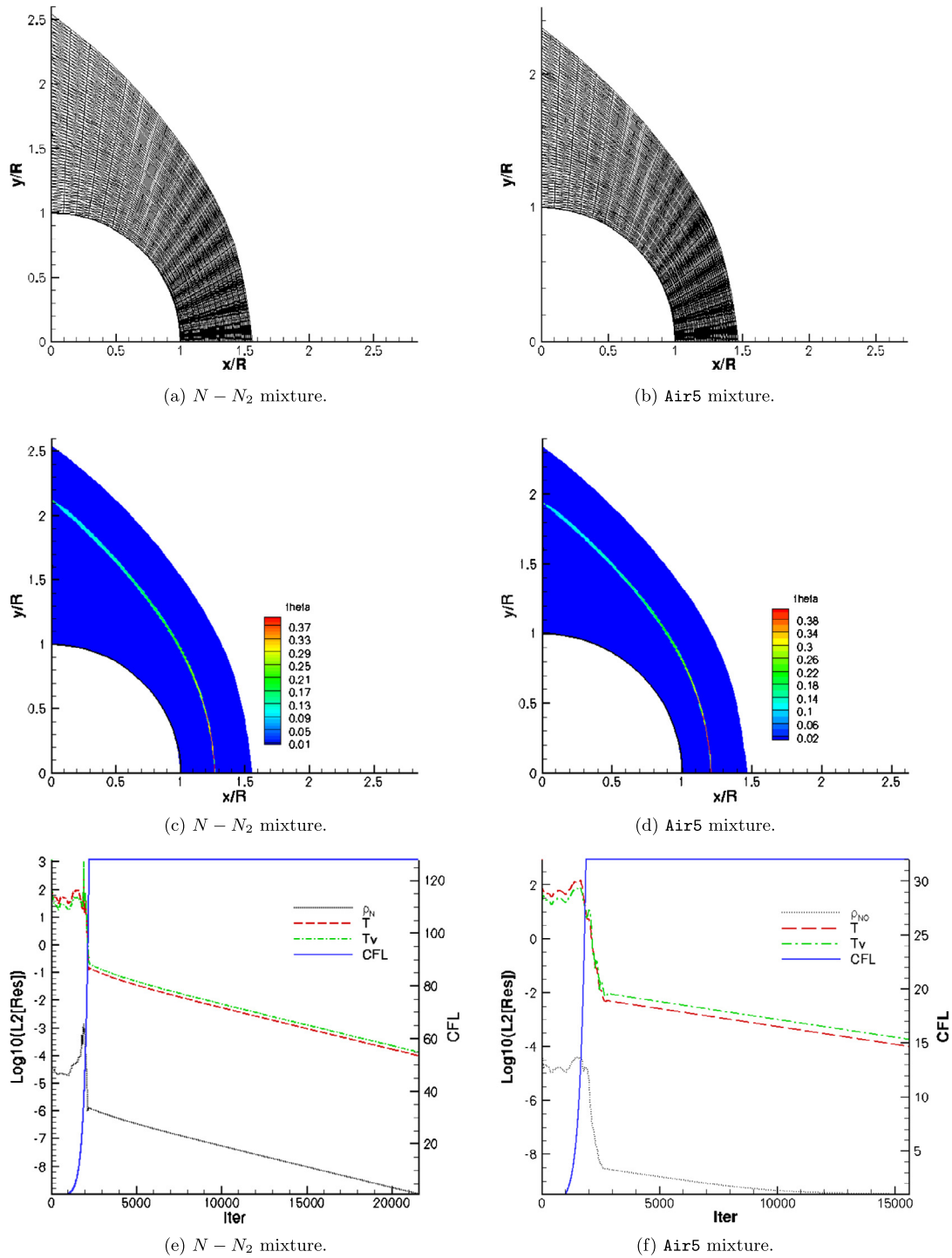


Fig. 2. Hypersonic inviscid TCNEQ flow around cylinder: in (a) and (b), meshes employed (only upper half and one out every fourth point shown); in (c) and (d): shock detector activation region; and in (e) and (f): convergence histories with Bcx scheme.

degrees of freedom. Figs. 2a and 2b present similar but coarser grids with $n_T \times n_R = 62 \times 33$ points. No sign of carbuncle was observed in these simulations, [23].

Figs. 2c and 2d shows the region where the shock detector is active, i.e. $\theta \in (0, 1]$. Note how in both cases the shock is captured across a very narrow region.

The Bcx solutions are restarted from a 1st order solution obtained with the Nc scheme. In both cases, the residual associated to the roto-translational temperature decreases six orders of magnitude, as seen in Figs. 2e and 2f.

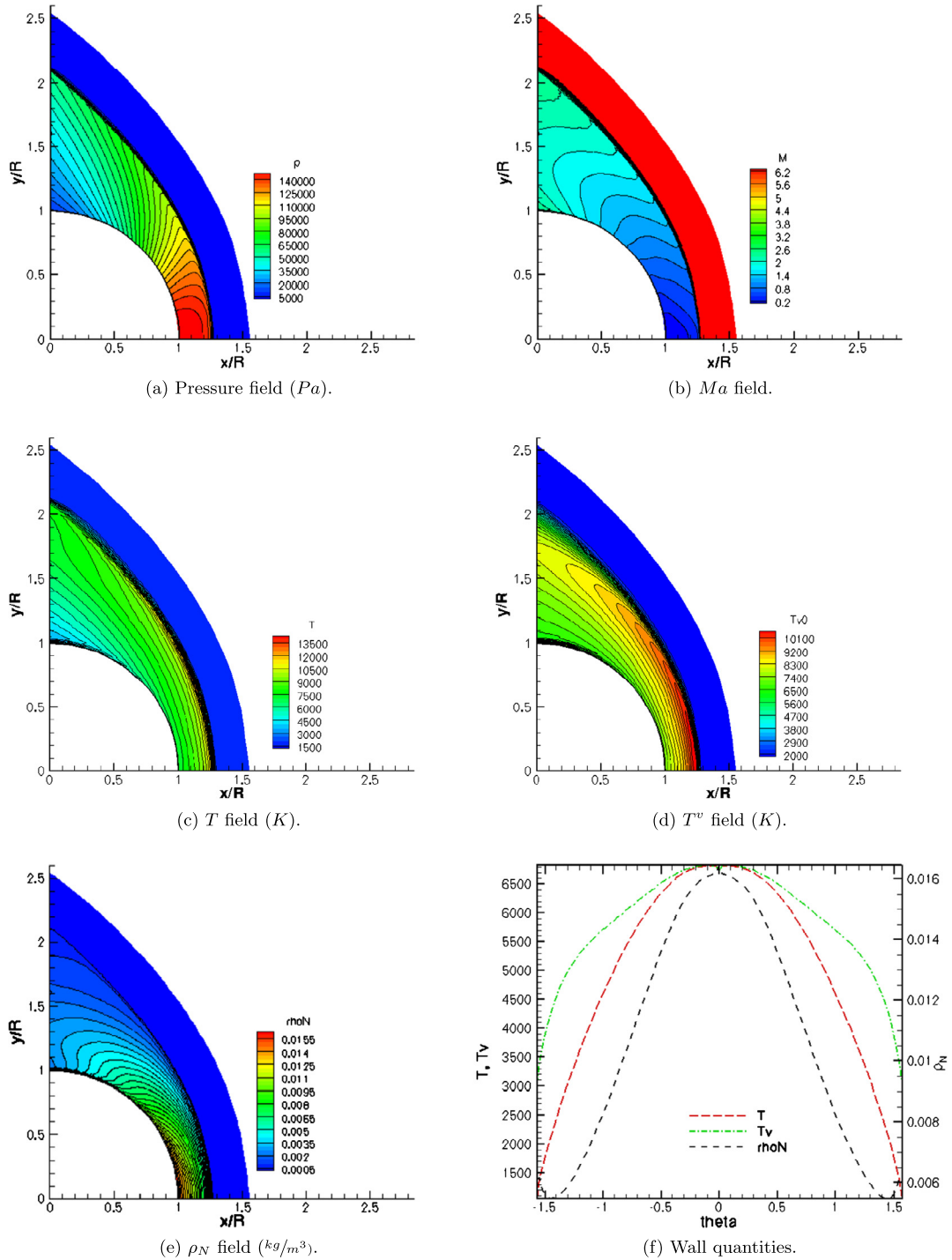


Fig. 3. Hypersonic inviscid TCNEQ flow around cylinder. $N - N_2$ mixture.

The results of the simulation for the $N-N_2$ mixture are gathered in Fig. 3. Note the strong compression in Fig. 3a. The effectivity of the additional shock dissipation term Eq. (60) is evident from the Mach number field in Fig. 3b: no overshoots of the Mach number are apparent.

Roto-translational and vibrational temperatures differ in the shock-layer, as is evident from Figs. 3c and 3d: the flow is in thermal non-equilibrium in the post-shock region.

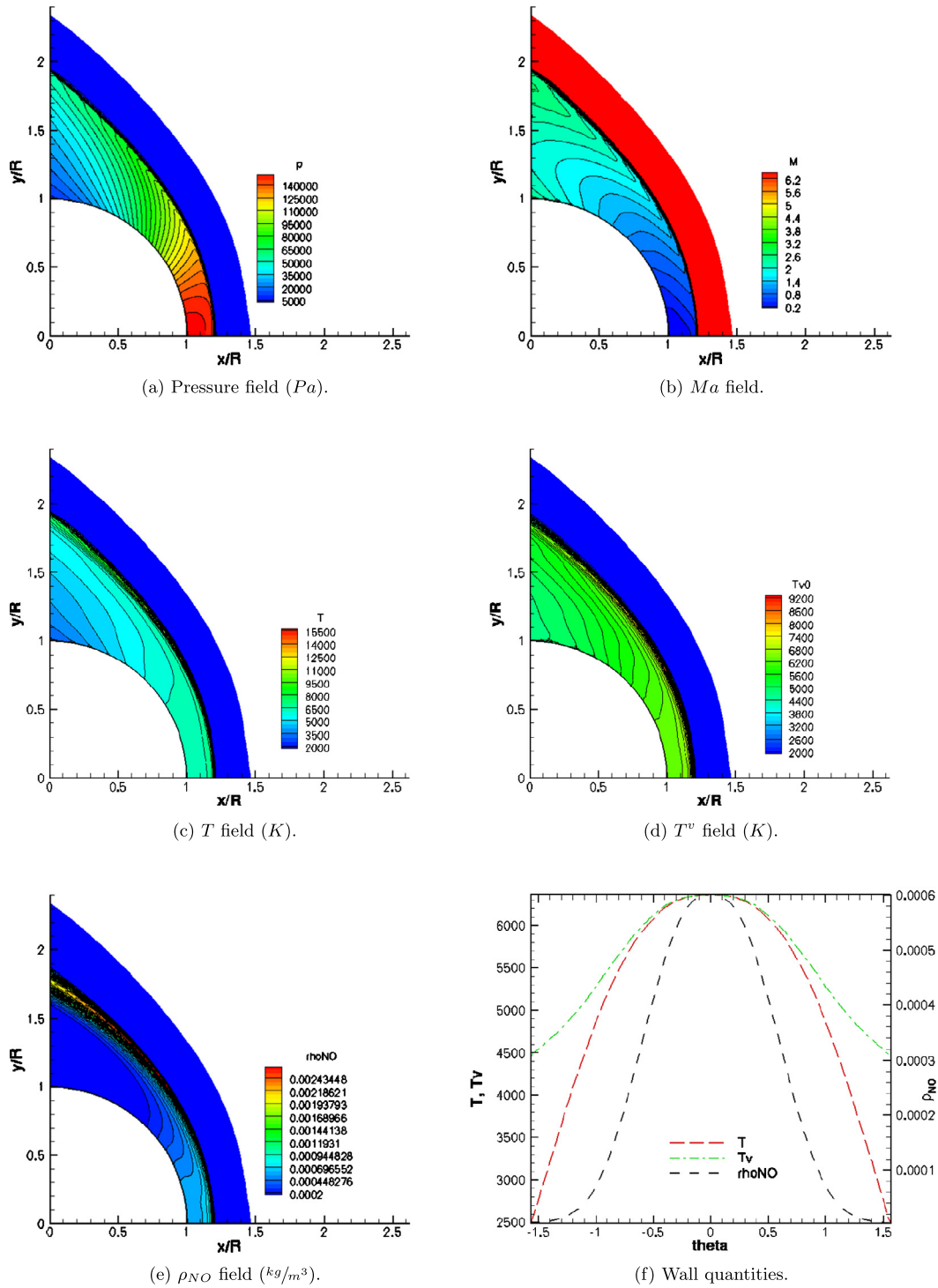


Fig. 4. Hypersonic inviscid TCNEQ flow around cylinder. *air5* mixture.

High temperatures in the post-shock region result as well in the dissociation of the molecular N_2 into atomic nitrogen, see Fig. 3e. Finally, Fig. 3f shows roto-translational and vibrational temperatures at the cylinder wall, together with atomic nitrogen density ρ_N .

Similar observations apply to the *Air5* simulation case, see Fig. 4. The compression across the shock wave is comparable to that of the $N - N_2$ mixture, Fig. 4a; however the temperature increase across the shock layer is much higher (Fig. 4c). Note also that less energy is trapped in the vibrational mode, Fig. 4d.

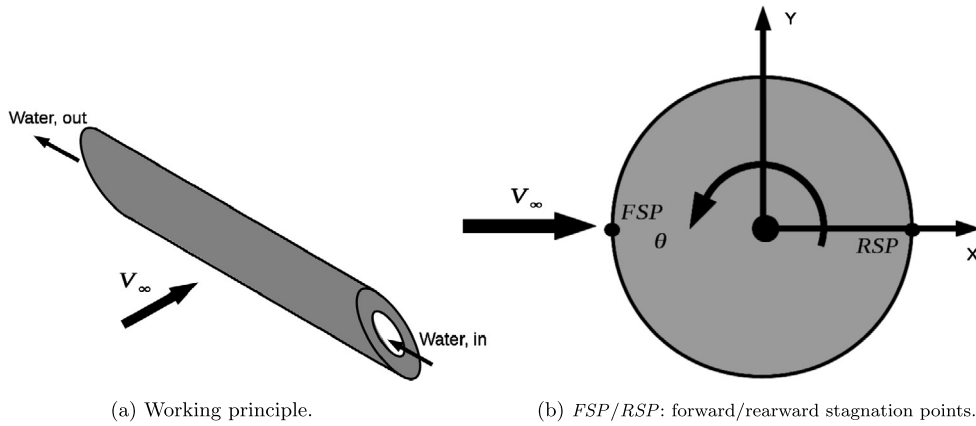


Fig. 5. Subsonic CNEQ flow around heat flux probe.

Table 3

Non-equilibrium Subsonic Flow around a Circular Cross-Section Probe. Testcase definition.

Ma_∞	ρ_∞ [kg/m ³]	p_∞ [Pa]	T_∞ [K]	T_{Wall} [K]
0.526	$4.8084e-04$	1500.	6000.	400.
Composition				
$y_{N,\infty}$ [-]	$y_{O,\infty}$ [-]	$y_{N_2,\infty}$ [-]	$y_{NO,\infty}$ [-]	$y_{O_2,\infty}$ [-]
0.5765	0.2326	$5.87e-04$	0.193	$3.72e-6$

Atomic components recombine to form nitric oxide, specially across the shock wave, Fig. 4e, and near the stagnation point, Fig. 4f.

5.2. Viscous CNEQ subsonic flow around cylindrical cross-section temperature probe

The second configuration (the first one accounting for viscous effects), consists of a cylindrical body (diameter $\phi = 8$ mm) placed transversely in an incoming hot subsonic air stream in chemical non-equilibrium. This configuration (see references [57,24]) corresponds to a heat flux probe employed into a high-enthalpy wind tunnel, Fig. 5a.

Wall quantities will be presented on the right-handed System of Reference (SoR) in Fig. 5b: $\theta \in (0, \pi)$ corresponds to the top wall of the cylinder, whereas the lower wall is defined by $\theta \in (-\pi, 0)$. For the top wall, $\theta = \pi$ is the forward stagnation point FSP, and $\theta = 0$ is the rearward stagnation point, RSP. For the lower wall, $\theta = -\pi$ is the FSP and $\theta = 0$ the RSP.

The computational domain is circular, with diameter $D = 72\phi$. An O-type mesh is employed, consisting of $n_{Dof} = 1.1 \times 10^4$ and $n_{Elem} = 2.2 \times 10^4$ triangular elements, see Fig. 6a. A far-field BC is imposed weakly at the outer boundary of the domain, while a no-slip isothermal wall BC is enforced at the cylinder wall.

The upstream conditions for this case (Table 3) are such that the molecular species are strongly dissociated, and hence chemical non-equilibrium has to be accounted for. Since the flow field is smooth (i.e. no shocks are present), the LDAC scheme (Eq. (50)) has been employed.

Residuals associated to the temperature and nitric oxide decreased by six orders of magnitude, see Fig. 6b. Figs. 6c–6d show the pressure and temperature fields. Notice the separation of the flow over the leeward side of the cylinder, in Fig. 6e: the symmetry of the recirculation in the separated region, expected in this kind of configuration, is evident. In this sense, the unstructured grid does not induce any spurious asymmetries as those reported e.g. in reference [76] for a non-reacting perfect gas case.

Fig. 6f compares the St distributions corresponding to the RD and FV [57,10] solutions: the heat flux predicted by the LDAC scheme agrees with the results in references over the region where the flow remains attached. There is a slight disagreement in the neighborhood of the FSP; the RD solution respects better the symmetry condition $\left. \frac{\partial q_w}{\partial \theta} \right|_{\pm\pi} = 0$.

The RD flow solution separates at $\theta \approx \pm 1$ rad (there where $Cf = 0$, not shown). Separation location depends greatly on the kinetic and thermophysical models employed; since the models provided by the MUTATION library differ from those used in [57], heating differences over the range $(-1.5, 1.5)$ rad in Fig. 6f come most likely from a difference in separation location.

Let us address the concern of *loss of accuracy* [52] linked to the P1 Galerkin discretization of the viscous terms (see appendix A). Nishikawa and Roe, in reference [52], described how the P1 Galerkin discretization strategy cannot maintain a uniform order of accuracy for the scalar advection–diffusion problem whenever the local Péclet number is nearby 1.

The behavior reported in [52] was also studied by other researchers, e.g. [77,6,7]. Specially relevant for us is the work of Villedieu and her collaborators [77]: they found out that reinterpreting RD schemes as SUPG methods, and then modulating

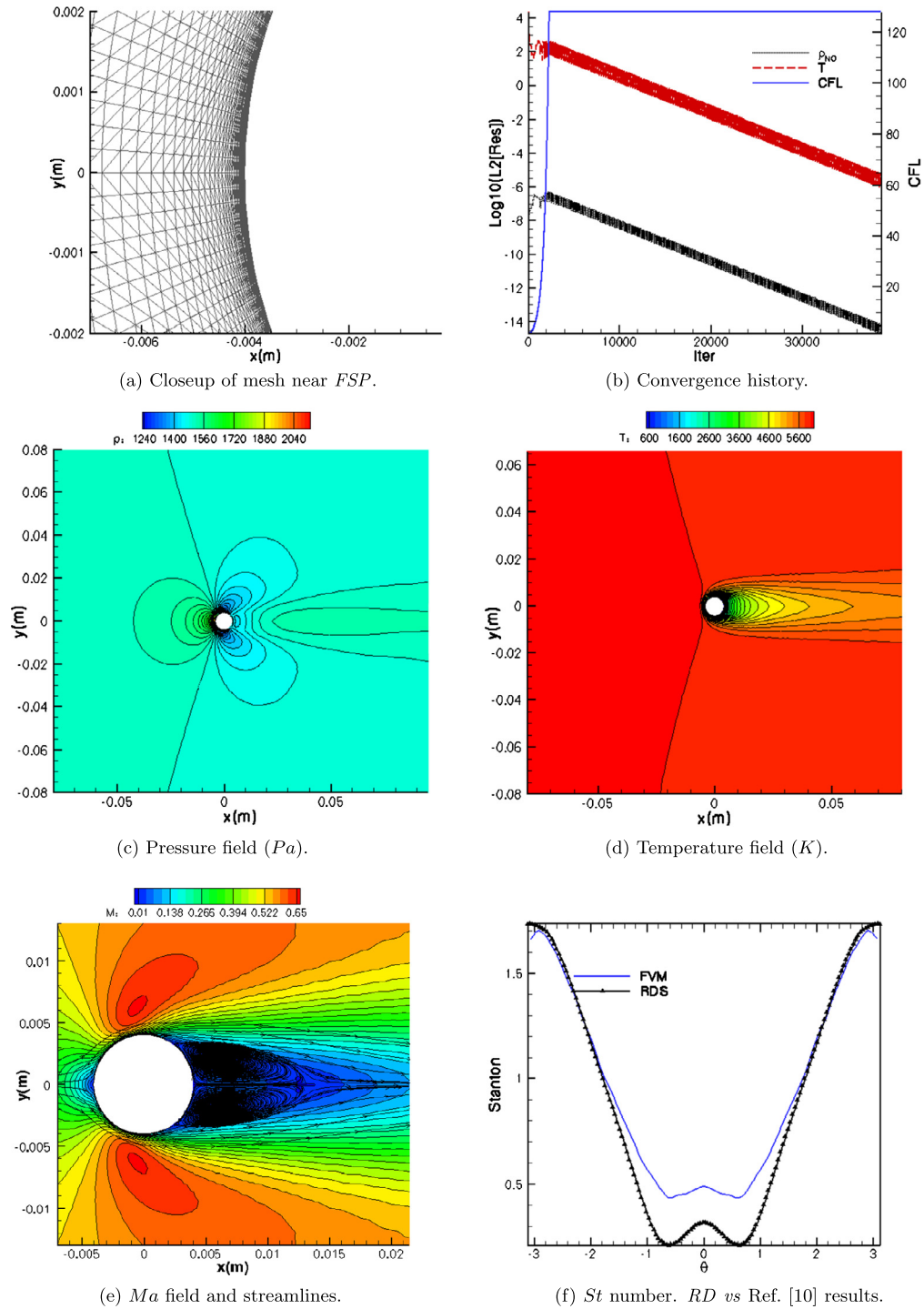


Fig. 6. Subsonic CNEQ flow around cylinder.

the upwind stabilization according to the local *Péclet* number it was possible to recover the correct order accuracy for the advection–diffusion case.

As for the Navier–Stokes equations, Villedieu et al. point out in [77,76] that for Reynolds numbers beyond a critical $Re^* \approx 60$, including the *Péclet*-based correction was not necessary.

For this first viscous problem, one can estimate a $Re \approx 24$ [57], which is below the Re^* identified by Villedieu. However, the agreement between our predicted heat flux results and independently retrieved experimental and computational

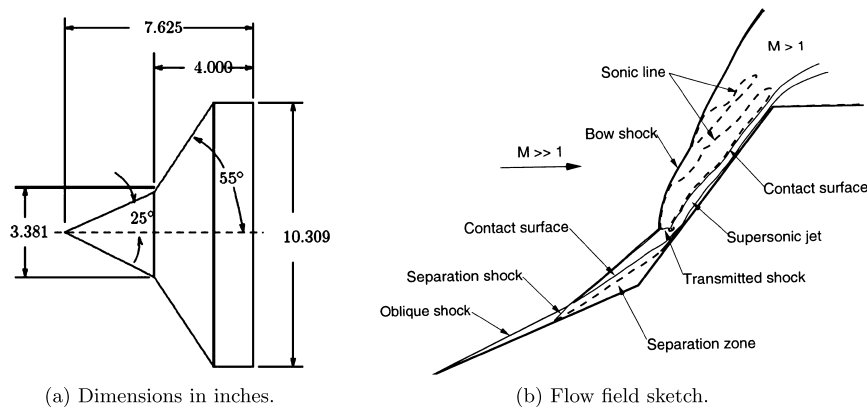


Fig. 7. Hypersonic TCNEQ flow around double cone configuration: in (a), model tested in LENS I shock tunnel; in (b), schematic flow field in *run 42* at high free stream enthalpy conditions (courtesy from [53]).

Table 4
non-equilibrium Hypersonic Flow around Double-Cone. Testcase definition.

Ma_∞	ρ_∞ [kg/m ³]	u_∞ [m/s]	T_∞ [K]	T_∞^v [K]	$y_{N,\infty}$ [–]	$y_{N_2,\infty}$ [–]
11.5	0.001468	3849.3	268.7	3160.	0	1

data [57,10] arise as a strong indication that both the computed solution and its gradients (∇T , but also ∇h_s) have been accurately retrieved.

5.3. Viscous TCNEQ hypersonic flow around double cone

We finally consider the high-enthalpy ($H_\infty = 9.17$ MJ/kg) and high-speed ($Ma_\infty = 11.5$) nitrogen flow over a double cone configuration [41]. This configuration has been analyzed within the RTO Task Group 43 (topic no 2) [36], which focused on a further assessment of *CFD* for the specific issue of shock interactions and control surfaces in non-equilibrium flows. Extensive experimental studies have also been conducted for this case in the LENS I shock tunnel at Calspan University of Buffalo Research Center (CUBRC) to obtain detailed surface and flow characteristics.

A sketch of a typical hypersonic flow field around a double cone is depicted in Fig. 7b; the full description of the complex shock wave/boundary layer interaction pattern can be found, e.g., in references [40,53].

An accurate prediction of the aerodynamic field and related quantities (heat flux) for hypersonic double cone flows requires thermo-chemical non-equilibrium effects to be taken into account, as demonstrated in [54,53,46]. Both reference literature and experimental data are available for the selected testcase, indicated as *run 42* in [53]. The nominal free stream conditions are listed in Table 4. Additionally, the wall temperature was set to 294.7 K. Since the Reynolds number for this configuration is relatively high ($Re \approx 6.35 \times 10^4$, [36]), the loss of accuracy problem is not a concern in this case.

The $N - N_2$ nitrogen mixture was used to model the chemistry. Only the second-order accurate results, computed with *Bcx*⁶ and Dobeš' shock detector are discussed here. The 256×512 points mesh (made of triangles) used is presented in Fig. 8a. The results which are reported next and are fully described in reference [41], were obtained by running till both the surface pressure distribution (and in particular the separation bubble size) and the surface heat flux stopped changing. The maximum allowable CFL was limited to 15.

From the roto-translational temperature and Mach number iso-contours in Figs. 8c–8e, the excellent shock-capturing properties of the CRD method are evident. The vibrational temperature of molecular nitrogen is shown in Fig. 8d, clearly indicating a non-negligible presence of thermal non-equilibrium in the flow, particularly in the boundary layer and downstream the bow shock, where the roto-translational temperature is higher.

Only a moderate dissociation of molecular nitrogen into atoms occurs, as highlighted from the iso-contours of atomic nitrogen mass fractions. Because of the effect of the vibration-dissociation coupling, the regions characterized by the highest vibrational temperature exhibit more chemical dissociation.

Fig. 9 show the comparison between experimental and computed heat flux and surface pressure. Specifically the latter quantities, which are of actual engineering interest, demonstrate the accurate prediction capabilities of the CRD solver.

⁶ The supplementary dissipation term $\delta^{Diss,D} = \delta^{Diss,LxF}$ has not been necessary for the double cone testcase.

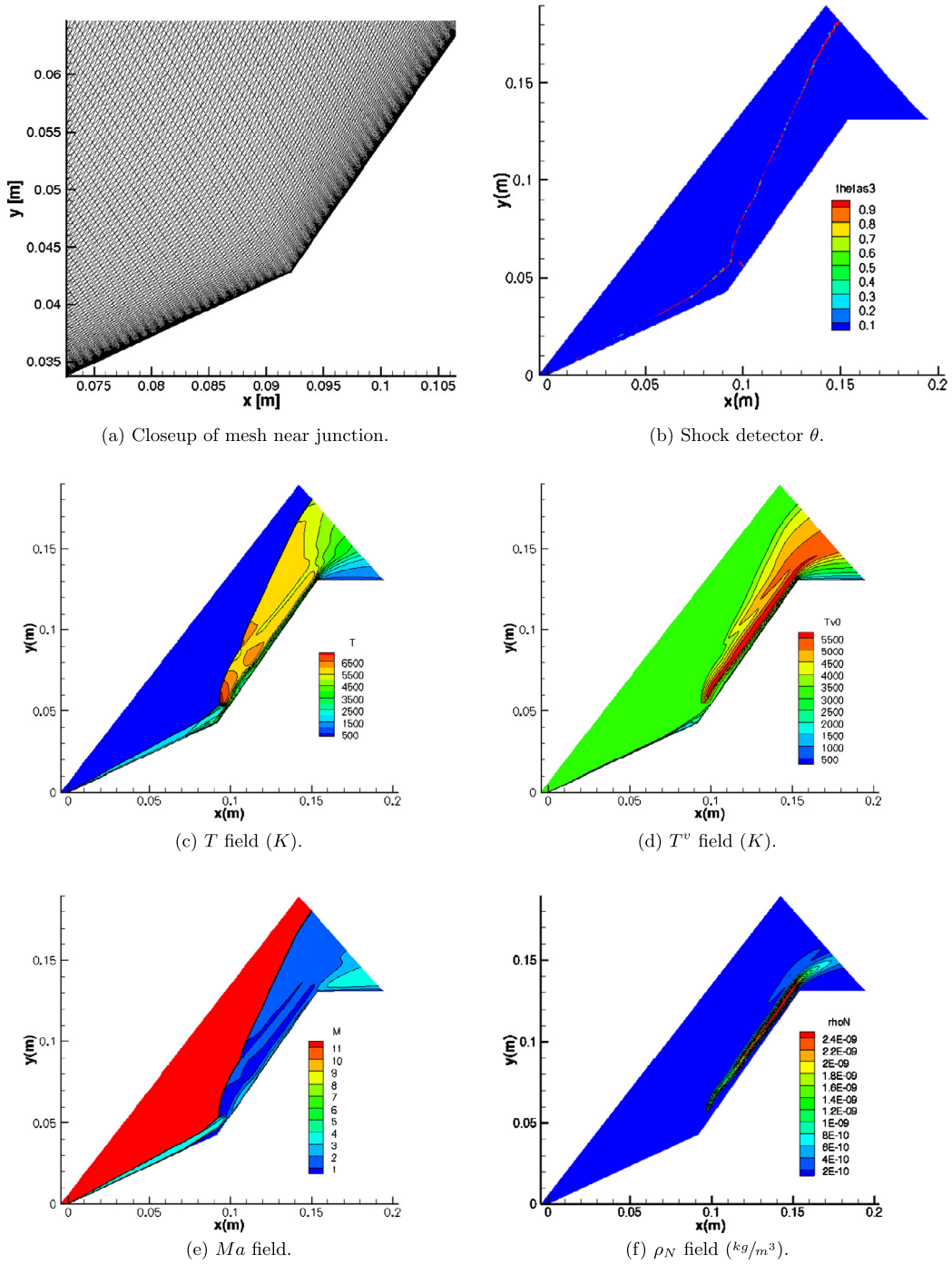


Fig. 8. Hypersonic TCNEQ flow around double cone configuration.

5.4. Performance evaluation

We reconsider now the testcases described in sections 5.1–5.3, and evaluate on them the computational advantage brought by performing the distribution of the convective residuals in the symmetrizing variables formulation described in 3.2. This advantage is quantified as:

$$\eta = \frac{t_{\text{Cons}} - t_{\text{Symm}}}{t_{\text{Cons}}} \times 100.0\% \quad (68)$$

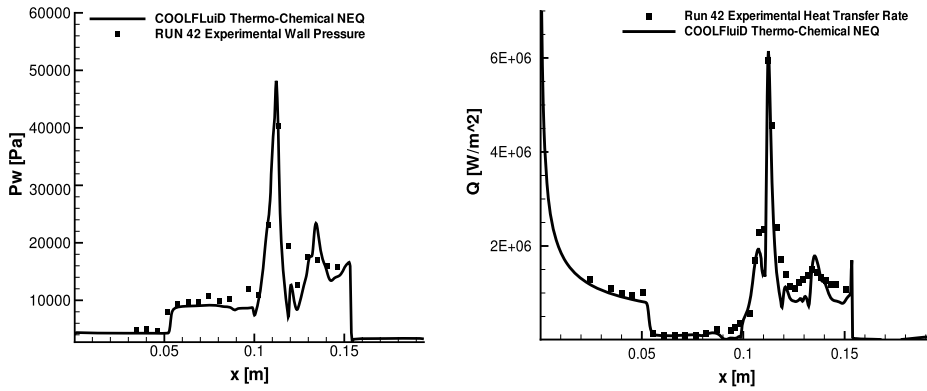


Fig. 9. Hypersonic TCNEQ flow around double cone configuration: wall quantities computed with Bcx scheme on triangular mesh with $n_{DoF} = 256 \times 512$. In (a) computed surface pressure vs. experimental measurements; in (b), computed surface heat flux vs experimental measurements.

Table 5

Hypersonic inviscid TCNEQ flow around cylinder: average time-per-iteration and efficiency improvement.

	N_2 -N mixture [s]	η [%]	air5 mixture [s]	η [%]
Cons. variables, NEQ	66.29	—	131.72	—
Symm. variables, NEQ	56.63	14.57	90.99	30.92
Cons. variables, frozen	21.35	—	60.96	—
Symm. variables, frozen	11.46	46.32	24.97	59.04
$n_{Iterations}$	21573			15594

Table 6

Subsonic CNEQ flow around cylinder: average time-per-iteration and efficiency improvement.

	air5 mixture [s]	η [%]
Cons. variables, NEQ	67.93	—
Symm. variables, NEQ	60.80	10.50
Cons. variables, frozen	42.48	—
Symm. variables, frozen	36.46	14.17
$n_{Iterations}$	38572	

where t_{Cons} and t_{Symm} are the average times spent on an iteration if the distribution is performed either in conservative or in symmetrizing variables, respectively.

The solution retrieved using the new set of symmetrizing variables is the same as the one obtained performing the convective residual distribution in conserved variables: this guarantees the correctness of the implementation. The total number of iterations is also the same, irrespective of the convective distribution strategy employed.

The following benchmarks have been performed on a computer equipped with an 8-core Intel(R) Xeon(R) E5-2609 CPU at 2.40 GHz, a cache memory of 10420 kB and 32 GB of RAM.

As described in appendix A, the advection and the source term residuals are typically distributed together. In order to precisely quantify the computational effort invested in the advective (and diffusive, for the viscous cases) evaluation and distribution from those corresponding to the source term, the computational advantage has also been evaluated on frozen conditions. Despite a frozen flow representation is not adequate for characterizing the flows considered, this frozen assumption is nevertheless useful to segregate the computational effort invested in the advective (and diffusive, for the viscous cases) residual evaluation and distribution from those corresponding to the source term: setting $\vec{S} = 0$ saves the (computationally intensive, see [56]) determination of thermochemical properties D_s , $k_{r,f}$, $k_{r,f}$ and τ_s .

The results obtained for the inviscid hypersonic cylinder, the subsonic viscous cylinder and the hypersonic double cone are summarized in Tables 5, 6 and 7 respectively. In all cases considered, a reduction in time-per-iteration is observed. This reduction is never below 10% (15%) for NEQ (frozen) case, and it is higher for frozen conditions, as expected. Note also that higher reductions are consistently obtained for Air5 mixtures, confirming that the larger n_s the greater the saving η attained. This is coherent with the observation in section 3.2 that only an $(n_D + 1) \times (n_D + 1)$ matrix needs to be inverted in the symmetrizing variables formulation, as opposed to the $n_{Eq} \times n_{Eq}$ matrix (with $n_{Eq} = n_s + n_D + 2$) for the standard formulation.

Note also that symmetrization yields a reduced benefit for viscous cases if compared to inviscid cases. This is due to the relative high computational cost of the diffusive fluxes (for mass, momentum and energy) using the accurate transport

Table 7
Hypersonic TCNEQ flow around double cone: average time-per-iteration and efficiency improvement.

	N_2 - N mixture [s]	η [%]
Cons. variables, NEQ	398.22	—
Symm. variables, NEQ	319.24	19.83
Cons. variables, frozen	279.72	—
Symm. variables, frozen	200.76	28.23
$n_{\text{Iterations}}$		20036

algorithms presented in [11,47]. The implementation of more conventional and simplified transport models could make the relative performance gain from symmetrization even more significant.

In summary, the computational advantage associated to distributing the advective residual in the symmetrizing variables has been quantified, showing that the larger the number of species in the mixture the larger the time reduction η will be. Additionally, the results obtained under the frozen flow assumption suggest that further reductions in η could be attained if – whenever it is physically justified – alternative strategies (e.g. precomputed look-up tables) are employed to determine the thermophysical/transport properties and the source term.

6. Conclusions

In this paper we have discussed the application of contour-integration-based Residual Distribution techniques to the simulation of inviscid and viscous flows in non-equilibrium conditions, considering flows in both the subsonic and hypersonic regimes. To this end, a general n_s species, two-temperature (roto-translational and vibrational-electronic) non-equilibrium thermophysical model has been considered. Second-order solutions have been obtained with Bcx scheme in combination with different shock sensors and, for the hypersonic cylinder cases only, the inclusion of extra dissipation in order to guarantee monotonicity.

Additionally, a transformation based on an entropy variable definition has been considered. This entropy transformation has been designed so that a symmetric structure of the projected advective Jacobian is obtained; on top of that, the transformed Jacobian presents a block diagonal structure where maximal decoupling is retrieved. Indeed, mass-species and electronic-vibrational energy terms are completely decoupled from the momentum and total-energy subsystem for the inviscid case.

The advantageous structure of the projected Jacobian allows to reduce the computational cost of the distribution of the advective residuals: established matrix distribution schemes can be substituted by hybrid matrix-scalar schemes. Hybrid matrix-scalar schemes offer the same result as the full-matrix schemes, but a fraction of the original cost: matrix operations in the hybrid matrix-scalar schemes involve matrices of much smaller dimension than in the original full-matrix case ($n_D + 1$ vs $n_S + n_D + 1$). This implies that the reduction in computing time increases with gas mixture complexity, i.e. with n_S .

Finally, despite in this contribution the entropy-variable-based transformation has been applied for shock-capturing computations with Residual Distribution schemes, nothing in the formulation prevents its application in other contexts, e.g. still in combination with Residual Distribution techniques but in a shock-fitting environment [55,59,38], or in combination with Finite Volume [29], Stabilized Finite Element [34] or Discontinuous Galerkin [12,60] schemes.

Acknowledgements

First author has been supported by a Belgian FRIA fellowship from the *Fonds National de la Recherche Scientifique*; and by the European Commission Research and Innovation action DRAGY (GA-690623). The assistance of the personnel of VKI Computer Center is gratefully acknowledged.

First author is grateful beyond words to Ms. E. Iorfida Gil for her support.

Appendix A. Further details on Residual Distribution Schemes

This appendix presents additional details on the residual distribution solver employed in this work.

A.1. Diffusive residual

Since the components of the diffusive flux tensor, \bar{F}_j^y depend not only on the solution \bar{U} but on its gradient as well:

$$\bar{F}_j^y = f(\mu, \lambda, \bar{U}, \nabla \bar{U}), \quad (69)$$

its discretization with $P1$ finite elements can be accomplished with Galerkin discretization:

$$\bar{\Phi}_l^d = \int_{\Omega} N_l \frac{\partial \bar{F}_j^v}{\partial x_j} dv = \int_{\Xi_l} N_l \frac{\partial \bar{F}_j^v}{\partial x_j} dv = \sum_{\Omega_i \in \Xi_l} \int_{\Omega_i} N_l \frac{\partial \bar{F}_j^v}{\partial x_j} dv. \quad (70)$$

Integration by parts and application of Gauss–Ostrogradsky theorem transform previous equation into:

$$\bar{\Phi}_l^d = \oint_{\Xi_l \cap \delta\Omega} N_l \bar{F}_j^v 1_j^{ext} ds - \sum_{\Omega_i \in \Xi_l} \int_{\Omega_i} \frac{\partial N_l}{\partial x_j} \bar{F}_j^v dv. \quad (71)$$

First term on the *RHS* of last equation is relevant only for elements lying on the external boundary, $\delta\Omega \cap \Xi_l \neq \emptyset$. Second term on the *RHS* collects the diffusive contributions to the nodal residual. The discrete form, for a *P1* linear element, is:

$$\bar{\Phi}_l^d = - \sum_{\Omega_i \in \Xi_l} \frac{1}{2} n_{j,l} \bar{F}_j^v \left(\mu_{avg}, \lambda_{avg}, \bar{U}_{avg}, \nabla \bar{U}^h \right). \quad (72)$$

Viscosity μ_{avg} and thermal conductivity λ_{avg} are evaluated at the average of the \vec{W} variables (see [41]), where $\vec{W} = [\rho_s, u_j, T, T^v]^t$.

Galerkin discretization of the diffusive term is consistent with *RD* discretization of the advective part presented in section 4.1 if one resorts to a Petrov–Galerkin interpretation of the *RD* methods [72,19,21], employing a trial function of the form:

$$\omega_l = N_l + \sum_{\Omega_i \in \Xi_l} \left(B_l^{\Omega_i} - \bar{I}_{nEqS} \right) \mathfrak{C}^{\Omega_i}, \quad (73)$$

where \mathfrak{C}^{Ω_i} is piecewise constant function of unit value in Ω_i and 0 everywhere else.

A.2. Source term residual

The source term contribution to the nodal residual $\mathfrak{f}^S \left(\bar{\Phi}^{S, \Omega_i} \right)$ in equation (40) is derived through a variational principle applied to the source term \bar{S} :

$$\bar{\Phi}_l^S = \int_{\Omega} \omega_l \bar{S} dv. \quad (74)$$

Straightforward manipulations reduce previous equation to:

$$\bar{\Phi}_l^S = \int_{\Xi_l} \omega_l \bar{S} dv = \sum_{\Omega_i \in \Xi_l} \int_{\Omega_i} \omega_l \bar{S} dv. \quad (75)$$

If a one-point quadrature rule is employed, Eq. (75) in discrete form is:

$$\bar{\Phi}_l^S = \sum_{\Omega_i \in \Xi_l} \Omega_i \omega_l(\vec{x}_g) \bar{S}(\vec{x}_g), \quad (76)$$

where \vec{x}_g is the center of mass of the simplicial element Ω_i .

In this manner, it is possible to define distribution matrices for the source term:

$$B_l^{\Omega_i, S} = \frac{1}{\Omega_i} \int_{\Omega_i} \omega_l dv. \quad (77)$$

Typically, $B_l^{\Omega_i, S}$ is chosen to coincide with the distribution matrix for the advective term, if such a matrix exists. For the particular case of the *Nc* scheme, the *LDAC* distribution matrix is employed [62,37].

A.3. Boundary conditions

References [19,5] present detailed considerations on boundary condition enforcement in the context of residual distribution schemes. Here, we discuss briefly the difference between strongly/weakly imposed boundary conditions and its relation to the limited subset of *BC*'s employed in this work.

A boundary condition is imposed *strongly* when the *a priori* known value of the solution is substituted into Eq. (38), so that:

$$\vec{U}^h(\vec{x}, t) = \sum_{j \in \delta\Omega^{h,D}} \vec{U}_j^{BC} N_j(\vec{x}) + \sum_{j \in \Omega^h - \delta\Omega^{h,D}} \vec{U}_j N_j(\vec{x}). \quad (78)$$

Alternatively, BC's can be enforced *weakly*, by adding a residual $\vec{\Phi}_l^{BC}$ to equation (40). This $\vec{\Phi}_l^{BC}$ is designed so that the solution \vec{U}_l at steady state reduces to the requested value \vec{U}_l^{BC} . The rationale for this technique departs from the weak formulation of the problem:

$$\int_{\Omega} \omega_l \frac{\partial \vec{F}_j}{\partial x_j} dv = \vec{0}.$$

Integration by parts, application of Gauss–Ostrogradsky theorem, and yet again integration by parts recast the problem as:

$$\int_{\Omega} \omega_l \frac{\partial \vec{F}_j}{\partial x_j} (\vec{U}^h) dv + \underbrace{\oint_{\delta\Omega} \omega_l [\vec{F}_j(\vec{U}^{h,BC}) - \vec{F}_j(\vec{U}^h)] 1_j^{ext} ds}_{\vec{\Phi}_l^{BC}} = \vec{0}. \quad (79)$$

Discretization of interior points is recovered but contributions from boundary conditions is now explicit. Equation (79) can be integrated numerically, or alternatively it can be cast in linearized form:

$$\vec{\Phi}_l^{BC} = \sum_{S_f \in \delta\Xi_l \cap \delta\Omega_{S_f}} \int \omega_l^{\delta\Omega_i} A_j^{c,U} (\vec{U}^{h,BC} - \vec{U}^h) 1_j^{ext} ds = K_l \cdot (\vec{U}_l^{BC} - \vec{U}_l^h). \quad (80)$$

RD schemes being a vertex-centered numerical technique, strong imposition of boundary conditions is straightforward there where the solution is fully known a priori, namely for the cases of no-slip (adiabatic/isothermal) walls and supersonic inlets. Nodes on a supersonic outlet region are treated as interior points, in agreement with characteristic lines leaving the domain.

Conversely, whenever the state vector cannot be defined unambiguously neither from the interior solution nor from external information, weak enforcement of the boundary condition is the natural alternative, specially if the *upwind projector* K_l^+ is used in Eq. (80) instead of K_l . The *upwind projector* discriminates information entering the domain while discards contributions associated to outgoing characteristics: this is the principle supporting weak far-field BC. Inviscid walls are also enforced weakly, but through Eq. (79). The flow tangency condition is imposed by specifying:

$$\Delta \vec{F}_j^c \equiv \vec{F}_j^{c,BC} - \vec{F}_j^{c,h} = -[\rho u_n, \rho u_j u_n, \rho E u_n]^t. \quad (81)$$

Symmetry is achieved simply by setting the vertical velocity component v to 0 in \vec{U}_l^{BC} , see [72].

A.4. Numerical solution of the discretized set of equations

Since system of equations (14) is of mixed parabolic–hyperbolic type, [30], its steady solution can be obtained marching in pseudo-time. The distribution procedure described in sections 4.1, A.1 and A.2 leads to the definition of a system of ordinary differential equations controlling the time evolution of the solution at the grid nodes. For the l -th node, it reads:

$$V_{\Xi_l} \frac{d\vec{U}_l}{dt} + \vec{\Phi}_l^c - \vec{\Phi}_l^d - \vec{\Phi}_l^s = \vec{0}, \quad (82)$$

where V_{Ξ_l} stands for the volume of the median dual cell around l -th node.

The discretization of Eq. (82) is accomplished by means of the COOLFLUID solver, described in [40]. Equation (82) is marched in pseudo-time until a steady state solution is reached, by using an implicit backward Euler integrator. The linear system of equations obtained at each *pseudo-time* step is then solved by one of the Krylov subspace methods [68] provided by the PETSc solver library [67].

All thermophysical properties and non-equilibrium terms are provided by the MUTATION library (see [56] for more details on the physico-chemical modeling aspects). As far as boundary conditions are concerned, isothermal wall and supersonic inlet boundary conditions are enforced strongly, whereas far-field, subsonic outlet and inviscid wall boundary conditions are imposed weakly, as detailed in [72].

References

- [1] COOLFLUID, <https://github.com/andrealani/COOLFLUID/wiki>. (Accessed 1 July 2017).
- [2] A. Lani, J. Garicano-Mena, H. Deconinck, A residual distribution method for symmetrized systems in thermochemical nonequilibrium, in: Number AIAA 2011-3546, 20th AIAA Computational Fluid Dynamics Conference, Honolulu, Hawaii, June 2011.
- [3] R. Abgrall, Toward the ultimate conservative scheme: following the quest, J. Comput. Phys. 167 (2001) 277–315.
- [4] R. Abgrall, M. Mezine, Construction of 2nd-order accurate monotone and stable RDS for steady flow problems, J. Comput. Phys. 195 (2004) 474–507.

- [5] R. Abgrall, D. De Santis, Linear and non-linear high order accurate residual distribution schemes for the discretization of the steady compressible Navier–Stokes equations, *J. Comput. Phys.* (ISSN 0021-9991) 283 (2015) 329–359, <https://doi.org/10.1016/j.jcp.2014.11.031>, <http://www.sciencedirect.com/science/article/pii/S0021999114007931>.
- [6] R. Abgrall, A. Larat, M. Ricchiuto, Construction of very high order residual distribution schemes for steady inviscid flow problems on hybrid unstructured meshes, *J. Comput. Phys.* 230 (2011) 4103–4136, <https://doi.org/10.1016/j.jcp.2010.07.035>.
- [7] R. Abgrall, D. De Santis, M. Ricchiuto, High-order preserving residual distribution schemes for advection–diffusion scalar problems on arbitrary grids, *SIAM J. Sci. Comput.* 36 (3) (2014) 955–983.
- [8] R. Abgrall, P. Bacigaluppi, S. Tokareva, A high-order nonconservative approach for hyperbolic equations in fluid dynamics, *Comput. Fluids* (ISSN 0045-7930) (2017), <https://doi.org/10.1016/j.compfluid.2017.08.019>, <http://www.sciencedirect.com/science/article/pii/S0045793017302906>.
- [9] J.D. Anderson, *Hypersonic and High Temperature Gas Dynamics*, 2nd ed., AIAA Textbooks Series, American Institute of Aeronautics and Astronautics, 2006.
- [10] P.F. Barbante, *Accurate and Efficient Modelling of High Temperature Nonequilibrium Air Flows*, PhD thesis, Université Libre de Bruxelles, 2001.
- [11] P.F. Barbante, G. Degrez, G.S.R. Sarma, Computation of nonequilibrium high-temperature axisymmetric boundary-layer flows, *J. Thermophys. Heat Transf.* 16 (2002) 490–497, <https://doi.org/10.2514/2.6723>.
- [12] E.G. Barter, D.L. Darmofal, Shock capturing with PDE-based artificial viscosity for DGfEM: Part I. Formulation, *J. Comput. Phys.* 229 (2010) 1810–1827, <https://doi.org/10.1016/j.jcp.2009.11.010>.
- [13] Aldo Bonfiglioli, Marco Grottadaurea, Renato Paciorri, Filippo Sabetta, An unstructured, three-dimensional, shock-fitting solver for hypersonic flows, *Comput. Fluids* 73 (2013) 162–174.
- [14] G.V. Candler, H.B. Johnson, I. Nompelis, P.K. Subbareddy, T.W. Drayna, V. Gidzak, M.D. Barnhardt, Development of the US3D Code for Advanced Compressible and Reacting Flow Simulations, in: Number AIAA 2015-1893, 53rd AIAA Aerospace Sciences Meeting, Florida, January 2015.
- [15] F. Chalot, T.J.R. Hughes, F. Shakib, Symmetrization of conservation laws with entropy for high temperature hypersonic computations, *Comput. Syst. Eng.* 1 (1990) 495–521.
- [16] A.J. Chorin, J.E. Marsden, *A Mathematical Introduction to Fluid Mechanics*, 3rd edition, Springer, 2000.
- [17] A. Csik, M. Ricchiuto, H. Deconinck, Conservative formulation of the multidimensional upwind residual distribution schemes for general nonlinear conservation laws, *J. Comput. Phys.* 179 (1) (2002) 286–312.
- [18] H. Deconinck, P.L. Roe, R. Struijs, A multidimensional generalization of Roe's flux difference splitter for the Euler equations, *Comput. Fluids* 22 (2–3) (1993) 215–222.
- [19] H. Deconinck, M. Ricchiuto, K. Sermeus, Introduction to residual distribution schemes and stabilized finite elements, LS 2003-05, VKI, 2003.
- [20] G. Degrez, E. van der Weide, Upwind Residual Distribution Schemes for Chemical Non-Equilibrium Flows, *Collection of Technical Papers*, vol. 2, AIAA, 1999, pp. 978–987.
- [21] J. Dobeš, M. Ricchiuto, R. Abgrall, H. Deconinck, On hybrid residual distribution-Galerkin discretizations for steady and time dependent viscous laminar flows, *Comput. Methods Appl. Mech. Eng.* 283 (2015) 1336–1356.
- [22] J. Garicano-Mena, On the Computation of Heat Flux in Hypersonic Flows Using Residual Distribution Schemes, PhD thesis, Université Libre de Bruxelles, 2014.
- [23] J. Garicano-Mena, A. Lani, H. Deconinck, An energy-dissipative remedy against carbuncle: application to hypersonic flows around blunt bodies, *Comput. Fluids* (ISSN 0045-7930) 133 (2016) 43–54, <https://doi.org/10.1016/j.compfluid.2016.03.028>, <http://www.sciencedirect.com/science/article/pii/S0045793016300858>.
- [24] Jesús Garicano-Mena, Raffaele Pepe, Andrea Lani, Herman Deconinck, Assessment of heat flux prediction capabilities of residual distribution method: application to atmospheric entry problems, *Communications in Computational Physics* (ISSN 1991-7120) 17 (3) (2015) 682–702, <https://doi.org/10.4208/cicp.070414.211114a>, http://journals.cambridge.org/article_S1815240615000146.
- [25] V. Giovangigli, *Multicomponent Flow Modelling*, Birkhäuser, Boston, 1999.
- [26] P. Gnoffo, R. Gupta, J. Shinn, Conservation equations and physical models for hypersonic air flows in thermal and chemical non-equilibrium, TP 2867, NASA, 1989.
- [27] P.A. Gnoffo, Upwind-biased, point-implicit relaxation strategies for viscous, hypersonic flows, in: *Proceedings of the 37th AIAA Aerospace Science Meeting and Exhibit*, Portland (OR), AIAA, 2004.
- [28] P.A. Gnoffo, Multi-dimensional, inviscid flux reconstruction for simulation of hypersonic heating on tetrahedral grids, in: *Proceedings of the 47th AIAA Aerospace Science Meeting and Exhibit*, Orlando (FL), AIAA, 2009.
- [29] P.A. Gnoffo, Updates to multi-dimensional flux reconstruction for hypersonic simulations on tetrahedral grids, in: *Proceedings of the 48th AIAA Aerospace Science Meeting and Exhibit*, Orlando (FL), AIAA, 2010.
- [30] C. Hirsch, *Numerical Computation of Internal and External Flows: Introduction to the Fundamentals of CFD*, 2nd edition, Butterworth-Heinemann, 2006.
- [31] J.O. Hirschfelder, C.F. Curtiss, R.B. Bird, *The Molecular Theory of Gases and Liquids*, second edition, Wiley, 1964.
- [32] T.J.R. Hughes, M. Mallet, A new finite element formulation for computational fluid dynamics: III. The generalized streamline operator for multidimensional advective–diffusive systems, *Comput. Methods Appl. Mech. Eng.* 58 (3) (1986) 305–328.
- [33] T.J.R. Hughes, M. Mallet, A new finite element formulation for computational fluid dynamics: IV. A discontinuity-capturing operator for multidimensional advective–diffusive systems, *Comput. Methods Appl. Mech. Eng.* 58 (3) (1986) 329–336.
- [34] B.S. Kirk, Adiabatic shock capturing in perfect gas hypersonic flows, *Int. J. Numer. Methods Fluids* 64 (2010) 1041–1062.
- [35] B.S. Kirk, G.F. Carey, Development and validation of a SUPG finite element scheme for the compressible Navier–Stokes equations using a modified inviscid flux discretization, *Int. J. Numer. Methods Fluids* 57 (2008) 265–293.
- [36] D. Knight, et al., Assessment of CFD capability for prediction of hypersonic shock interactions, *Prog. Aerosp. Sci.* (ISSN 0376-0421) 48–49 (2012) 8–26, <https://doi.org/10.1016/j.paerosci.2011.10.001>, <http://www.sciencedirect.com/science/article/pii/S0376042111001023>.
- [37] A. Lani, *An Object Oriented and High-Performance Platform for Aerothermodynamic Simulations*, PhD thesis, Université Libre de Bruxelles, 2008.
- [38] A. Lani, V. De Amicis, SF: an open source object-oriented platform for unstructured shock-fitting methods, in: M. Onofri, R. Paciorri (Eds.), *Shock Fitting, in: Shock Wave and High Pressure Phenomena*, 2017.
- [39] A. Lani, H. Deconinck, Conservative residual distribution method for hypersonic flows in thermochemical nonequilibrium, in: *Proceedings of the 47th AIAA Aerospace Science Meeting and Exhibit*, Orlando (FL), AIAA, 2009.
- [40] A. Lani, N. Villedieu, K. Bensassi, L. Kapa, M. Vymazal, M.S. Yalim, M. Panesi, COOLfluid: an open computational platform for multi-physics simulation and research, in: AIAA 2013-2589, San Diego (CA), June 2013, 21th AIAA CFD Conference.
- [41] A. Lani, M. Panesi, H. Deconinck, Conservative residual distribution method for viscous double cone flows in thermochemical nonequilibrium, *Commun. Comput. Phys.* 13 (2013) 479–501.
- [42] A. Larat, Conception et analyse de schémas d'ordre très élevé distribuant le résidu: application à la mécanique des fluides, PhD thesis, Université de Bordeaux I, 2009.
- [43] P.D. Lax, Weak solutions of nonlinear hyperbolic equations and their numerical computation, *Commun. Pure Appl. Math.* (ISSN 1097-0312) 7 (1) (1954) 159–193, <https://doi.org/10.1002/cpa.3160070112>.

- [44] R.J. Leveque, Finite Volume Methods for Hyperbolic Problems, Cambridge University Press, 2002.
- [45] Y. Liu, M. Vinokur, Upwind algorithms for general thermo-chemical nonequilibrium flows, in: Proceedings of the 27th AIAA Aerospace Science Meeting and Exhibit, Reno(NV), AIAA, 1989.
- [46] M. MacLean, M. Holden, T. Wadhams, R. Parker, A computational analysis of thermochemical studies in the LENS facilities, in: Number AIAA 2007-0121, 45th AIAA Aerospace Sciences Meeting and Exhibit, Reno, Nevada, January 2007.
- [47] Thierry E. Magin, Gérard Degrez, Transport properties of partially ionized and unmagnetized plasmas, Phys. Rev. E 70 (2004) 046412, <https://doi.org/10.1103/PhysRevE.70.046412>.
- [48] A. Mazaheri, H. Nishikawa, Very efficient high-order hyperbolic schemes for time-dependent advection–diffusion problems: Third-, fourth-, and sixth-order, Comput. Fluids 102 (2014) 131–147.
- [49] A. Mazaheri, H. Nishikawa, High-order shock-capturing hyperbolic residual–distribution schemes on irregular triangular grids, Comput. Fluids 131 (2016) 131–147, <https://doi.org/10.1016/j.compfluid.2016.03.012>.
- [50] A. Mazaheri, P.A. Gnoffo, C.O. Johnston, W.L. Kleb, LAURA Users Manual, Technical Report TM-2013-217800, NASA Langley Research Center, 2013.
- [51] NASA. FUN3D, <http://fun3d.larc.nasa.gov/>. (Accessed 20 August 2014).
- [52] H. Nishikawa, P.L. Roe, On high-order fluctuation-splitting schemes for the Navier–Stokes equations, in: Proceedings of the 3rd International Conference on Computational Fluid Dynamics, Toronto, July 2004, ICCFD.
- [53] I. Nompelis, Computational Study of Hypersonic Double-Cone Experiments for Code Validation, PhD thesis, University of Minnesota, 2004.
- [54] I. Nompelis, T.W. Drayna, G.V. Candler, A parallel implicit solver for hypersonic reacting flow simulation, in: Number AIAA 2005-4867, 17th Computational Fluid Dynamics Conference, Toronto, Canada, June 2005.
- [55] R. Paciorri, A. Bonfiglioli, A shock-fitting technique for 2D unstructured grids, Comput. Fluids 38 (2009) 715–726.
- [56] M. Panesi, Physical Models for Nonequilibrium Plasma Flow, PhD thesis, Università degli studi di Pisa, 2009.
- [57] S. Paris, B. Bottin, V. Van Der Haegen, M. Carbonaro, Determination of temperature profiles in plasma jets with a crossflow tube probe, in: Proceedings of the AIAA 34th Thermophysics Conference, Denver, 2000, AIAA, 2000.
- [58] C. Park, Nonequilibrium Hypersonic Aerothermodynamics, Wiley-Interscience, 1990.
- [59] R. Pepe, A. Bonfiglioli, A. D'Angola, G. Colonna, R. Paciorri, An unstructured shock-fitting solver for hypersonic plasma flows in chemical non-equilibrium, Comput. Phys. Commun. 196 (2015) 179–193, <https://doi.org/10.1016/j.cpc.2015.06.005>.
- [60] P.O. Persson, J. Peraire, Sub-cell shock capturing for discontinuous Galerkin methods, AIAA Pap. 2006 (2006) 112.
- [61] S.S. Rao, The Finite Element Method in Engineering, 5th edition, Butterworth-Heinemann, 2005.
- [62] M. Ricchiuto, Construction and Analysis of Compact Residual Distribution Discretizations for Conservation Laws on Unstructured Meshes, PhD thesis, Université Libre de Bruxelles, 2005.
- [63] M. Ricchiuto, N. Villedieu, R. Abgrall, H. Deconinck, On uniformly high-order accurate residual distribution schemes for advection–diffusion, in: Proceedings of the Third International Conference on Advanced Computational Methods in Engineering, ACOMEN 2005, J. Comput. Appl. Math. (ISSN 0377-0427) 215 (2) (2008) 547–556, <https://doi.org/10.1016/j.cam.2006.03.059>, <http://www.sciencedirect.com/science/article/pii/S0377042706007667>.
- [64] P. Roe, Linear Advection Schemes on Triangular Meshes, Coa, Cranfield Institute of Technology, 1987.
- [65] P.L. Roe, Approximate Riemann solvers, parameter vectors, and difference schemes, J. Comput. Phys. 43 (1981) 357–372.
- [66] V.V. Rusanov, The calculation of the interaction of non-stationary shock waves and obstacles, USSR Comput. Math. Math. Phys. (ISSN 0041-5553) 1 (2) (1962) 304–320, [https://doi.org/10.1016/0041-5553\(62\)90062-9](https://doi.org/10.1016/0041-5553(62)90062-9), <http://www.sciencedirect.com/science/article/pii/0041555362900629>.
- [67] J. Brown, S. Balay, Petsc Users Manual, Technical Report ANL-95/11 – Revision 3.4, Argonne National Laboratory, 2013.
- [68] Y. Saad, Iterative Methods for Sparse Linear Systems, second edition, SIAM, 2003.
- [69] K. Sermeus, Multi-Dimensional Upwind Discretization and Application to Compressible Flows, PhD thesis, Université Libre de Bruxelles, 2013.
- [70] K. Sermeus, H. Deconinck, Solution of steady Euler and Navier–Stokes equations using residual distribution schemes, LS 2003-05, VKI, 2003.
- [71] R. Struijs, H. Deconinck, P. Roe, Fluctuation splitting for multidimensional convection problems: an alternative to finite volume and finite element methods, LS 1990-04, VKI, 1990.
- [72] E. van der Weide, Compressible Flow Simulation on Unstructured Grids Using Multi-Dimensional Upwind Schemes, PhD thesis, Technische Universiteit Delft, 1998.
- [73] E. van der Weide, H. Deconinck, Positive matrix distribution schemes for hyperbolic systems of with applications to the Euler equations, in: Proceedings of the 3rd European CFD Conference, Paris, 1996, pp. 747–753.
- [74] E. van der Weide, H. Deconinck, E. Issman, G. Degrez, A parallel, implicit, multi-dimensional upwind, residual distribution method for the Navier–Stokes equations on unstructured grids, Comput. Mech. 23 (2) (1999) 199–208.
- [75] D. Vanden Abeele, An Efficient Computational Model for Inductively Coupled Air Plasma Flows under Thermal and Chemical Non-Equilibrium – with Application to Atmospheric Re-Entry Flow Studies, PhD thesis, Katholieke Universiteit Leuven, 2000.
- [76] N. Villedieu, High Order Discretisation by Residual Distribution Schemes, PhD thesis, Université Libre de Bruxelles, 2009.
- [77] N. Villedieu, T. Quintino, M. Ricchiuto, H. Deconinck, Third order residual distribution schemes for the Navier–Stokes equations, J. Comput. Phys. 230 (11) (2011) 4301–4315, <https://doi.org/10.1016/j.jcp.2010.12.026>, <http://www.sciencedirect.com/science/article/pii/S002199911000700X>, Special issue High Order Methods for CFD Problems.
- [78] M.J. Wright, G.V. Candler, D. Bose, Data-parallel line relaxation method for the Navier–Stokes equations, AIAA J. 36 (9) (1998) 1603–1609.